ANNALS OF GEOPHYSICS, 69, 2, SA224, 2026; doi:10.4401/ag-9415
OPEN ACCESS

Low-Latitude Ionospheric Responses to Two Matched Intense Equinoctial Geomagnetic Storms: A Case-Based Comparison Between Solar Cycles 24 and 25

Chollada Pansong[1] and Prasert Kenpankho[*,2]

(1) Department of Technical Education, Faculty of Technical Education, Rajamangala University of Technology Thanyaburi, Pathum Thani, 12110, Thailand

(2) Department of Engineering Education, School of Industrial Education and Technology, King Mongkut's Institute of Technology Ladkrabang, Bangkok, 10250, Thailand

Article history: received August 27, 2025; accepted February 13, 2026

Abstract

This study investigates the ionospheric responses to two matched intense equinoctial geomagnetic storms that occurred during Solar Cycles 24 and 25 (SCs 24 and 25), with emphasis on variations in Total Electron Content (TEC), the F2-layer critical frequency (foF2), and the F2-layer peak height (hmF2). TEC data were derived from Global Ionospheric Maps (GIMs) based on Global Navigation Satellite System (GNSS) observations, while foF2 and hmF2 parameters were obtained from the Global Assimilative Model of the Bottomside Ionosphere Timeline (GAMBIT) for 22 low-latitude locations worldwide. The results show that the SC25 storm produced stronger and more spatially extensive ionospheric responses than the SC24 event. Peak TEC values during SC25 exceeded those of SC24 by up to ~80-90 TECU in the Southeast Asian, East Asian, and Pacific sectors near the storm main phase, indicating a pronounced positive ionospheric storm. These enhancements are closely associated with higher solar wind speeds (~650-700 km s^{-1}) and strongly fluctuating IMF Bz during SC25, which generated sustained multi-pulse Prompt Penetration Electric Fields (PPEFs) that intensified E × B plasma drifts and the equatorial fountain effect. In contrast, SC24 was characterized by lower solar wind speeds (~550-600 km s^{-1}) and a predominantly southward IMF Bz, resulting in shorter-lived PPEF activity, weaker TEC enhancements, and pronounced depletion during the recovery phase. Correlation analysis between Dst and TEC disturbances reveals strong negative correlations ($r \approx -0.6$ to -0.9) in the Asia-Pacific sectors during the main phase, indicating that enhanced TEC disturbances tend to coincide with periods of increasing storm intensity, whereas predominantly positive correlations ($r \approx 0.6$-0.9) are observed in the Middle Eastern-African-European sector, reflecting TEC depletion. The foF2 response shows clear phase dependence, with localized daytime enhancements during the main phase but widespread reductions of ~15-20% during recovery in both solar cycles, consistent with the influence of Disturbance Dynamo Electric Fields (DDEFs), and thermospheric composition changes. In contrast, hmF2 exhibits solar-cycle-dependent behavior, with modest increases (~3-8%) during SC24 and more variable, often negative responses (up to ~2-3% decrease) during SC25. These findings highlight the heterogeneous, region-dependent, and solar cycle-dependent nature of ionospheric variability during intense geomagnetic storms, with important implications for space weather modeling and prediction.

Keywords: Geomagnetic storms; Solar cycle; TEC; foF2; hmF2

1. Introduction

Global Navigation Satellite Systems (GNSS) rely on signal quality that is affected by variations in the density of electrons in the ionosphere, which acts as a propagation medium, altering the signal's phase and amplitude (Chernyshov et al., 2020). The Total Electron Content (TEC) significantly affects GNSS signals by introducing delays and distortions. Irregular plasma density can cause positioning errors or signal loss. Solar and geophysical forces, such as the Interplanetary Magnetic Field (IMF), solar wind, and geomagnetic storms that change the conditions of plasma near Earth, cause these ionospheric disturbances (Hofmann-Wellenhof et al., 1992; Pi et al., 1997; Skone et al., 2000; Chernyshov et al., 2020). Positive ionospheric storms increase electron density by altering the electric field and winds in the thermosphere. Conversely, most negative storms are caused by changes in the atmospheric composition (Serafimov et al., 1982; Nayak et al., 2016; Reddybattula et al., 2019). The TEC change depends on location, especially near the magnetic equator, where electromagnetic fields improve electrical conductivity (Li et al., 2019). When a geomagnetic storm occurs, heat from ionospheric currents and high-energy particles alters plasma density, making it harder for satellites in low Earth orbit to navigate. The ionosphere is divided into four regions: high, mid, low, and equatorial latitudes. The low-latitude region within ±30° geomagnetic latitude (Zhao et al., 2024) exhibits the highest electron density, particularly at the crests of the Equatorial Ionization Anomaly (EIA), and is characterized by complex phenomena such as the Equatorial Electrojet (EEJ) and the fountain effect (Timoçin, 2019; Picanço et al., 2022; Uga et al., 2024; Tariku, 2024). Previous studies have consistently shown that the low- and equatorial-latitude ionosphere is highly dynamic and responds strongly to geomagnetic storms through a combination of electrodynamic and thermospheric processes. Observations from GNSS-TEC, ionosondes, magnetometers, and satellite measurements demonstrate that storm-time variability in TEC and F-region parameters is primarily governed by the interplay of Prompt Penetration Electric fields (PPEF), Disturbance Dynamo Electric Fields (DDEF), and associated neutral wind and composition changes, which together modulate the EIA, pre-reversal enhancement, and plasma irregularity development (Kenpankho et al., 2011; Nava et al., 2016; Ray et al., 2017; Dias et al., 2020; Singh et al., 2021). Multi-longitudinal and regional studies further indicate that the same geomagnetic storm can produce contrasting positive and negative ionospheric responses depending on local time, latitude, and storm phase, with enhancements or depletions of TEC persisting from the main phase into recovery (Picanço et al., 2022; Habyarimana et al., 2023). Recent investigations during SC25 highlight that extreme storm events can drive TEC perturbations of unprecedented magnitude, while also revealing discrepancies between station-based observations and global ionospheric products or empirical models (Pansong et al., 2025; Can and Erdag, 2025).

The Sun's activity is linked to the SC. The track of the Sun's activity was counting sunspots. These are visible signs of the Sun's magnetic activity, which intensifies as the Sun's activity increases. They have a cycle of about 11 years with four stages: minimum, ascending, maximum, and descending. Sunspots are linked to phenomena such as solar flares, Coronal Mass Ejections (CMEs), and Stream Interaction Regions (SIRs). In addition, significant decreases in the Disturbance Storm Time (Dst) index are often associated with geomagnetic storms caused by CMEs. However, solar flares and swift solar wind from coronal craters may also have comparable effects on Earth's magnetosphere. (Reyes et al., 2021). The longest and deepest solar minimum in recent history occurred before SC24 (2008-2019) and exhibited a peculiar pattern of activity. From 2008 to 2010, solar activity was low for an extended period. Then, in late 2011, solar activity surged rapidly, peaking just before 2013, declining briefly, and peaking between 2014 and 2015. This significant minimum has been compared to a historical period of decreased solar activity, marked by few sunspots and significant global cooling (Solomon et al., 2010; Pesnell, 2016; Lazzús, 2022). Conversely, during the SC25 peak in 2021-2022, more sunspots and stronger particle streams will generate geomagnetic storms ranging from G1 to G5 (Can and Erdağ, 2025). During the SC25 ascending phase, intense geomagnetic storms will continue to affect TEC over low latitudes, mirroring trends from previous cycles while exhibiting characteristics related to this cycle's specific solar activity (Singh et al., 2021; Picanço et al., 2022; Wang et al., 2023). This results in increased TEC values due to high-energy particles and changes in neutral wind patterns, leading to ionospheric ionization. PPEFs from high latitudes quickly lift ionospheric plasma, leading to a rapid rise in TEC. DDEFs are caused by thermospheric winds that heat Joule heating, and they usually lower TEC several hours after a storm begins (Singh et al., 2021; Mošna et al., 2024; Tilahun et al., 2025). Geomagnetic storms also cause ionospheric anomalies such as plasma bubbles and flares, particularly near the equator, which lead to changes in TEC. During this period, GNSS receivers and ionosondes showed that TEC increased during the storm and decreased during the recovery. The effects are more potent at lower than at mid latitudes (Nava et al., 2016; Picanço et al., 2022).

Previous studies of the ionospheric response to severe geomagnetic storms show that TEC changes in complex ways due to electric fields, thermospheric winds, and compositional changes (Lazzús et al., 2022; Berényi et al., 2023; Paul et al., 2025). In the early stages of a storm, electron density usually increases, but at night it decreases rapidly due to plasma lift and significant alterations in the thermosphere (Dabas et al., 2006; Berényi et al., 2023). The mid-latitude ionospheric trough extending towards the equator, the stronger plasma movement, and irregularities such as scintillation all affect the accuracy of GNSS signals (Paul et al., 2025; Li et al., 2024). Regional studies illustrate spatial variability; for instance, Dabas et al. (2006) noted reductions in nighttime electron density at the equator and increases at lower latitudes in India, influenced by disturbed electric fields and neutral winds. During the 2015 St. Patrick's Day storm, Nava et al. (2016) found that TEC levels decreased at mid-latitudes but increased near the equator. Yadav et al. (2016) and Ray et al. (2017) showed that the geomagnetic storm of March 17-18, 2015, produced ionospheric detachment effects over the Indian sector. On March17, 2015 (main phase), foF2 decreased, and hmF2 did not show any uplift. TEC values increased during the daytime (positive storm) due to PPEF-driven plasma uplift and increased electron density. Conversely, on March 18, 2015 (recovery period), foF2 remained below the quiescent level, hmF2 was intermittent, and TEC decreased at night (negative storm) under the influence of DDEF, and the O/N_2 ratio decreased. Singh et al. (2021) found that TEC increased during the onset and recovery periods of flash storms. In contrast, the nighttime decrease was influenced by conflicting electric fields and local wind dynamics in India. Berényi et al. (2023) used multi-instrumental observations to monitor two large geomagnetic storms during SC24 in Europe. They showed that electron density fluctuations, manifested as nighttime electron depletion and daytime increase, were driven by plasma motion, the electric field, and the equatorial extension of the mid-latitude trough. Barad et al. (2025) examined the impact of a severe geomagnetic storm occurring on April 23-24, 2023, using multi-station GNSS-TEC, ionosonic observations, and TIE-GCM simulations. The study showed that PPEF, DDEF, and changes in the thermosphere's composition all contribute to storm-time variability. The results indicated that TEC significantly increased during the main phase and decreased significantly during the recovery phase, especially at night. Regional differences and hemispheric asymmetry further highlight the complex interplay between electrodynamic and atmospheric processes during geomagnetic disturbances. In addition, Bareh and Chetia (2025) studied how the ionosphere responded to the intense geomagnetic storm that occurred during solar maximum at SC24. They observed changes in electron density and critical frequency (foF2) at three Japanese stations: Okinawa, Kokubunji, and Wakkanai, located at low, middle, and high latitudes, respectively. The results showed a significant decrease in electron density at all stations, with foF2 decreasing by 40% to 70% and decreasing more at higher latitudes. In summary, these studies show how ionospheric, thermospheric, and plasmaspheric processes are all linked during geomagnetic storms.

This study provides a comprehensive case study examining ionospheric variations, including TEC, foF2, and peak height (hmF2) across various low-latitude regions globally during two significant, closely aligned geomagnetic storms that transpired on March 17-18, 2015, and April 23-24, 2023, corresponding to SC24 and SC25, respectively. This study employed a comprehensive multi-instrument approach by integrating TEC data derived from IONosphere map EXchange (IONEX) products, sampled at 22 low-latitude International GNSS Service (IGS) reference locations, with ionospheric parameters obtained from the IRI Real-Time Assimilative Mapping (IRTAM) model. This integrated framework was used to investigate the temporal and spatial variability of the low-latitude ionosphere and to improve the understanding and modeling of space weather effects in these regions.

2. Data and Methods

In our study, we focus on analyzing disturbances in the ionospheric F2 parameters during two coherent geomagnetic storm events, on March 17-18, 2015, and April 23-24, 2023, corresponding to SCs 24 and 25. We examined TEC variations over three days before and four days after a geomagnetic storm. This study analyzed IONEX-derived TEC sampled at 22 low-latitude locations corresponding to selected IGS coordinates. Additionally, foF2 and hmF2 parameters were obtained from the Global Assimilative Model of the Bottomside Ionosphere Timeline (GAMBIT), an online nowcasting system that provides global ionospheric conditions derived from the IRTAM 3-D assimilative model (Reinisch and Galkin, 2011). The IRTAM 3-D model assimilates real-time ionosonde measurements from the Global Ionosphere Radio Observatory (GIRO) network to produce model-based estimates of ionospheric parameters at the selected low-latitude locations. Geomagnetic storm events are classified based on physical measurements using the Kp and Dst indices, which are used to analyze changes in ionospheric parameters. These data are collected as follows:

2.1 TEC data

TEC values were extracted from the IONEX global ionospheric maps at 1-hour temporal resolution and sampled at geographic locations corresponding to selected IGS reference coordinates using spatial interpolation. The IONEX products were obtained from the NASA CDDIS archive (https://cddis.nasa.gov/archive/gnss/products/ionex/YYYY/DDD/). Each global ionospheric map has a spatial resolution of 2.5° in latitude and 5° in longitude. In total, 22 low-latitude IGS reference locations distributed worldwide were considered.

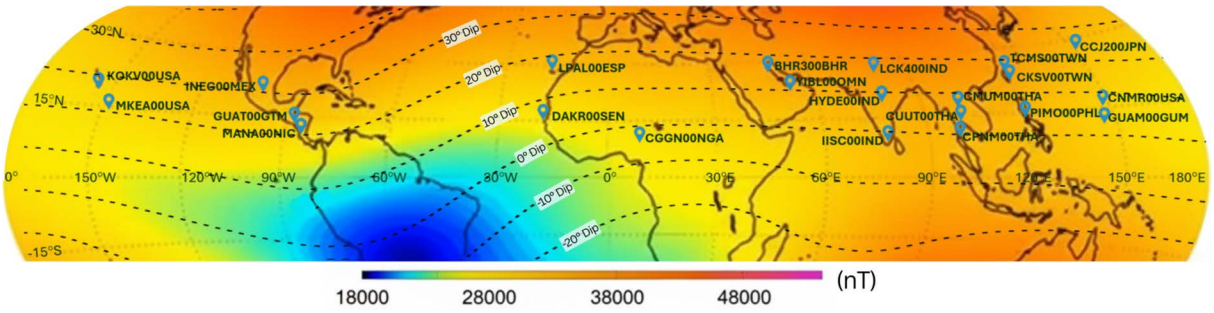

Figure 1. Geographic and geomagnetic distribution of the 22 low-latitude IGS reference locations used for sampling IONEX-derived TEC.

These locations were grouped into six longitudinal sectors to facilitate regional comparison of ionospheric TEC variability. Details are shown in Table 1.

Table 1. The 22 low-latitude GNSS locations, grouped by regional sectors, with their geographic coordinates.

Regional sectors	Locations	Latitude -Longitude
The American sector	KOKV00USA (Kokee Park, Waimea, USA) MKEA00USA (Mauna Kea, USA) INEG00MEX (Aguascalientes, Mexico) GUAT00GTM (Guatemala City, Guatemala) MANA00NIC (Managua, Nicaragua)	22.12°N, -159.66°E 19.80°N, -155.46°E 21.86°N, -102.28°E 14.59°N, -90.52°E 12.15°N, -86.25°E
The Middle Eastern-African-European sector	LPAL00ESP (Roque de los Muchachos, Spain) DAKR00SEN (Dakar, Senegal) GGN00NGA (Nigeria) BHR300BHR (Manama, Bahrain) YIBL00OMN (Yibal, Oman)	28.76°N, -17.89°E 14.72°N, -17.44°E 10.12°N, 9.12°E 26.21°N, 50.61°E 22.19°N, 56.11°E
The Indian sector	LCK400IND (Lucknow, India) HYDE00IND (Hyderabad, India) IISC00IND (Bangalore, India)	26.91°N, 80.96°E 17.42°N, 78.55°E 13.02°N, 77.57°E
The Southeast Asian sector	CMUM00THA (Chiang Mai, Thailand) CUUT00THA (Chulalongkorn University, Thailand) CPNM00THA (Chumphon, Thailand)	18.76°N, 98.93°E 13.74°N, 100.53°E 10.72°N, 99.37°E
The East Asian sector	TCMS00TWN (Hsinchu, Taiwan) CKSV00TWN (Tainan, Taiwan) PIMO00PHL (Quezon City, Philippines)	24.80°N, 120.99°E 23.00°N, 120.22°E 14.64°N, 121.08°E
The Pacific Ocean sector	CCJ200JPN (Ogasawara, Japan) CNMR00USA (Northern Mariana Islands, USA) GUAM00GUM (Dededo, Guam)	27.07°N, 142.20°E 15.23°N, 145.74°E 13.59°N, 144.87°E

The difference in TEC (dTEC) between SC24 and SC25 was calculated at each location (i) and each corresponding hourly epoch (t) within the analyzed 8-day storm window. dTEC was computed as the direct difference between the TEC during the SC25 event and that during the SC24 event, as expressed below:

$$dTEC(i,t) = TEC_{SC25}(i,t) - TEC_{SC24}(i,t) \quad (1)$$

Positive dTEC values indicate enhanced TEC during the SC25 storm relative to the SC24 storm, whereas negative values indicate reduced TEC during SC25. This formulation enables a direct storm-to-storm comparison under similar geomagnetic conditions, allowing us to highlight solar-cycle-dependent differences in ionospheric response without introducing normalization or quiet-time references.

In addition, the disturbance in TEC (ΔTEC) (Gordiyenko et al., 2025) is commonly used to analyze ionospheric disturbances. It is defined as the difference between the TEC at a given time and a reference TEC, typically derived from quiet-time conditions. The general form of the ΔTEC formula is given by:

$$\Delta TEC(t) = TEC(t) - TECq(t) \quad (2)$$

where TECq(t) represents the quiet-time reference TEC, defined as the mean TEC under geomagnetically quiet conditions.

Multi-day quiet references (commonly the mean or median of the five quietest days) have been widely adopted for TEC and VTEC storm analyses to reduce day-to-day variability and provide a local-time-matched baseline (e.g., Rukundo et al., 2023; Kim and Kwak, 2025). In addition, the sensitivity of storm-time responses to the choice of quiet reference is commonly evaluated by comparing alternative baseline definitions (e.g., Zhu et al., 2022). Zhu et al. (2022) calculated the difference between storm-day TEC and a quiet-time reference. The primary baseline was defined using the immediate pre-storm quiet day. To assess the robustness of the results, a five-day-averaged quiet baseline was also tested. The spatial and temporal TEC response patterns remained qualitatively unchanged, indicating that the results are not sensitive to the baseline choice. In this study, the quiet-time baseline was defined within the same six-day event window, excluding the storm interval. This event-centered approach minimizes seasonal and solar flux variability and enables a direct comparison between storm-time conditions and the immediate background state. All selected quiet days satisfied $Kp \leq 4$.

2.2 foF2 data

Temporal variations of the ionospheric foF2 parameter were analyzed at 22 selected low-latitude locations using the GAMBIT platform (Reinisch and Galkin, 2011). The analysis was performed by inputting the geographic coordinates of the selected locations into the GAMBIT system, which provides model-based ionospheric nowcasts derived from the IRTAM framework. The GAMBIT products assimilate real-time ionosonde measurements from the GIRO network and are accessible at https://giro.uml.edu/rix/gambit-local-nowcast/. Hourly foF2 data were obtained for both SC24 and SC25 events over an eight-day interval, including three days prior to and four days following each geomagnetic storm. Storm-time ionospheric responses were quantified relative to quiet-time conditions by computing the mean foF2 values over a six-day quiet interval and a two-day storm interval. The relative variation was subsequently expressed as a percentage change, as defined in Eq. (3).

$$\%\Delta foF2 = \frac{foF2_{storm} - foF2_{quiet}}{foF2_{quiet}} \times 100 \quad (3)$$

2.3 hmF2 data

The temporal behavior of the ionospheric hmF2 parameter was examined at 22 selected low-latitude locations using the GAMBIT platform (Reinisch and Galkin, 2011), which is accessible through the GIRO portal (https://giro.uml.edu/rix/gambit-local-nowcast/). The analysis was conducted by inputting the geographic coordinates of the selected locations into the GAMBIT system, which provides model-based ionospheric nowcasts derived from the IRTAM framework. Hourly hmF2 values were obtained for SCs 24 and 25 over an eight-day interval, including three days prior to and four days following each geomagnetic storm. Storm-time hmF2 responses were quantified relative to quiet-time conditions by computing mean hmF2 values over a six-day quiet interval and a two-day storm interval, with the relative variation calculated according to Eq. (4).

$$\%\Delta\mathrm{hmF2} = \frac{\mathrm{hmF2}_{\mathrm{storm}} - \mathrm{hmF2}_{\mathrm{quiet}}}{\mathrm{hmF2}_{\mathrm{quiet}}} \times 100 \tag{4}$$

2.4 Geomagnetic storm data

This study analyzes the impact on ionospheric parameters TEC, foF2, and hmF2 during two intense geomagnetic storms with Dst values lower than −200 nT. The first, most intense of SC24 occurred on March 17-18, 2015, and was called the St. Patrick's Day Storm. The National Oceanic and Atmospheric Administration (NOAA) classified the storm as a severe G4, with the Kp index reaching 8 three times on March 17, 2015, (12:00-15:00 UT, 15:00-18:00 UT, and 21:00-24:00 UT), with the main phase starting at 08:00 UT and the Dst index decreasing to −223 nT at 2 :00 UT (Wu et al., 2016; Ray et al., 2017; Habyarimana et al., 2023). A similar geomagnetic storm occurred during SC25, following a slight influence from an Interplanetary Coronal Mass Ejection (ICME) until April 20, 2023, and a minor disturbance on April 21, 2023. The first primary impulse arrived shortly before 17:00 UTC on April 23, 2023, in the form of an interplanetary shock wave: the fast-moving solar wind and the ensuing dramatic SIRs. However, the geomagnetic efficiency decreased at 22:00 UT due to the northward shift of the IMF, which prepared the magnetosphere for a strong southerly IMF (~40 nT) shock when the strong southerly IMF appeared at 01:00 UT on April 24, 2023, and remained in effect until 09:00 UT. This storm was classified as a moderate (G2) and severe (G4) storm, with a minimum Dst value of −212 nT at 05:00 UT on April 24, 2023, and a Kp index of 8− (Mošna et al., 2024; Rao et al., 2025). Hourly equatorial Dst values were obtained from the Kyoto WDC website (https://wdc.kugi.kyoto-u.ac.jp/dst_provisional/index.html). The Kp index data for geomagnetic storms comes from NOAA's Space Weather Prediction Center (SWPC) (https://www.swpc.noaa.gov/). Additionally, hourly Kp geomagnetic storm data are retrieved from the Pushkov Institute of Terrestrial Magnetism, Ionosphere, and Radio Wave Propagation (IZMIRAN) at https://www.izmiran.ru/ionosphere/weather/storm/. All solar wind and interplanetary parameters used in this study, including the PPEF, the interplanetary magnetic field component Bz, and the solar wind velocity (V), were retrieved from NASA's Space Physics Data Facility (SPDF). The data were downloaded from https://spdf.gsfc.nasa.gov/pub/data/omni/omni_cdaweb/hro2_5min/, a publicly accessible OMNI high-resolution archive. These datasets were analyzed and plotted in Fig. 2.

Figure 2 compares the variations of solar wind speed, IMF Bz, and PPEF associated with two geomagnetic storm events that occurred on March 17, 2015 (SC24) and April 24, 2023 (SC25). Although the two storms occurred in different solar cycles, they exhibit similar fundamental initiation mechanisms. In both cases, storm onset is associated with an increase in solar wind speed and a southward turning of the IMF Bz, which enhances solar wind-magnetosphere coupling and facilitates dayside magnetic reconnection. This process enables rapid penetration of magnetospheric convection electric fields into low latitudes in the form of PPEF, leading to intensification of the ring current and a sharp decrease in the Dst index, which marks the beginning of the storm main phase. For both events, the most rapid decreases in Dst coincide with intervals of strong southward Bz, and pronounced PPEF signatures are observed predominantly during the main phase, confirming the dominant role of IMF Bz-driven electrodynamic forcing in storm development. Despite these similarities, differences are evident in the magnitudes and temporal evolutions of the storm drivers between SC24 and SC25. During the SC24, the IMF Bz reached sustained southward values of approximately −15 to −20 nT, accompanied by enhanced solar wind speeds of about 550-600 km s^{-1}. These conditions produced efficient and sustained energy transfer into the magnetosphere, leading to rapid

Figure 2. Comparison of geomagnetic activity during SC24 and SC25 storm events, presented by the Dst index, hourly Kp index, PPEF, Bz, and V variations over time.

and intense storm development. In contrast, the SC25 was characterized by higher solar wind speeds, reaching approximately 650-700 km s^{-1}, but with a more variable IMF Bz that fluctuated strongly between southward and northward orientations, with minimum values of about −10 to −15 nT. The large and rapid swings of Bz during SC25 promoted frequent transitions between undershielding and overshielding conditions, leading to stronger, more persistent, and multi-pulse PPEF activity compared with the weaker and more sporadic PPEF pulses observed during

SC24. Differences between the two storms are also reflected in their storm-phase evolution, as indicated by the Dst index. The main phase of the SC25 storm is noticeably longer, characterized by a more gradual but sustained decrease in Dst, consistent with prolonged solar wind driving and highly fluctuating IMF Bz that maintained repeated PPEF forcing. In contrast, the SC24 storm exhibits a shorter but more abrupt main phase, reflecting stronger southward IMF conditions acting over a more limited time interval. During the recovery phase, SC25 shows a faster return of Dst toward quieter levels, whereas SC24 remains at more negative Dst values for a longer duration, indicating a slower decay of the ring current following the more intense southward IMF forcing in 2015. These results demonstrate that while the magnitude of southward IMF Bz primarily controls storm intensity, higher solar wind speeds and enhanced Bz variability, as observed in SC25, can prolong electrodynamic forcing and modulate the temporal evolution of geomagnetic storm phases.

3. Results

3.1 TEC variations

This section analyzes TEC variations during geomagnetic storms by examining temporal and spatial changes across 22 low-latitude locations grouped into eight longitudinal sectors. The results reveal distinct ionospheric response patterns in SC24 and SC25, reflecting the sensitivity of low-latitude TEC to geomagnetic disturbances as shown in Fig. 3.

Figure 3, based on a comparative analysis of geomagnetic storm events during SC24 (March 2015) and SC25 (April 2023), shows that the observed TEC variations can be consistently interpreted in terms of storm-time PPEF effects across different longitudinal sectors. Overall, the SC25 storm exhibits stronger and more sustained PPEF signatures during the main phase than SC24, acting as a more efficient electrodynamic driver that enhances E x B upward drifts in the equatorial F region. This process strengthens the equatorial fountain effect, leading to larger TEC enhancements across many low-latitude regions. The most pronounced TEC responses during SC25 are observed in the Southeast Asian and East Asian sectors, where dTEC values are predominantly positive and reach their largest magnitudes. At locations such as TCMS00 and CKSV00 in Taiwan and CMUM00 in Thailand, TEC peaks during the SC25 approach, reaching ~100-110 TECU near the storm main phase. In these regions, the main phase of SC25 coincides with local daytime conditions, allowing eastward PPEF to effectively intensify the development of the EIA crests, resulting in substantially higher electron densities than during SC24 at comparable local times. In the Indian sector, TEC enhancements during SC25 are more moderate but persist throughout the storm interval. TEC values remain consistently higher than those observed during SC24 during the initial, main, and recovery phases, with ΔTEC remaining predominantly positive into the recovery phase. This behavior suggests prolonged plasma uplift and retention associated with the stronger electrodynamic forcing during SC25. The Middle Eastern-African-European sector also shows enhanced TEC during SC25. Low-latitude locations such as CGGN00 and YIBL00 exhibit clear TEC increases, while mid-latitude locations in southern Europe (e.g., LPAL00) show larger enhancements during SC25 than during SC24. This pattern indicates a broader latitudinal redistribution of plasma from the magnetic equator toward higher latitudes under enhanced fountain conditions. In the Pacific Ocean sector, locations such as GUAM00 and CNMR00 record SC25 TEC values exceeding those of SC24 by approximately 20-30 TECU at peak times. Despite the oceanic setting, the enhanced PPEF during SC25 is sufficient to generate a pronounced positive ionospheric storm response, particularly during local daytime intervals. The American sector exhibits a distinct temporal behavior, with negative ΔTEC during the early stages of the event, likely associated with less favorable local-time conditions. As the storm progresses into the main phase, ΔTEC becomes positive, indicating that the stronger electrodynamic forcing during SC25 supports higher TEC levels once favorable local-time conditions are established.

Figure 4 illustrates the temporal and spatial variations of TEC during geomagnetic storm events in SC24 and SC25. A clear contrast is observed between the two events, with the SC25 storm producing significantly stronger, more widespread, and more persistent TEC enhancements than the SC24 storm. Pronounced TEC increases are evident during SC25 near the storm main phase across several locations in the Southeast Asian, East Asian, and Pacific regions, indicating the occurrence of a strong positive ionospheric storm. In contrast, the SC24 event exhibits weaker and less spatially coherent TEC responses, with some regions showing TEC reductions near peak storm activity. Both events display clear diurnal TEC variability; however, the amplitude of these variations is substantially larger during SC25. Overall, the results demonstrate that the geomagnetic storm in SC25 exerted a more effective ionospheric

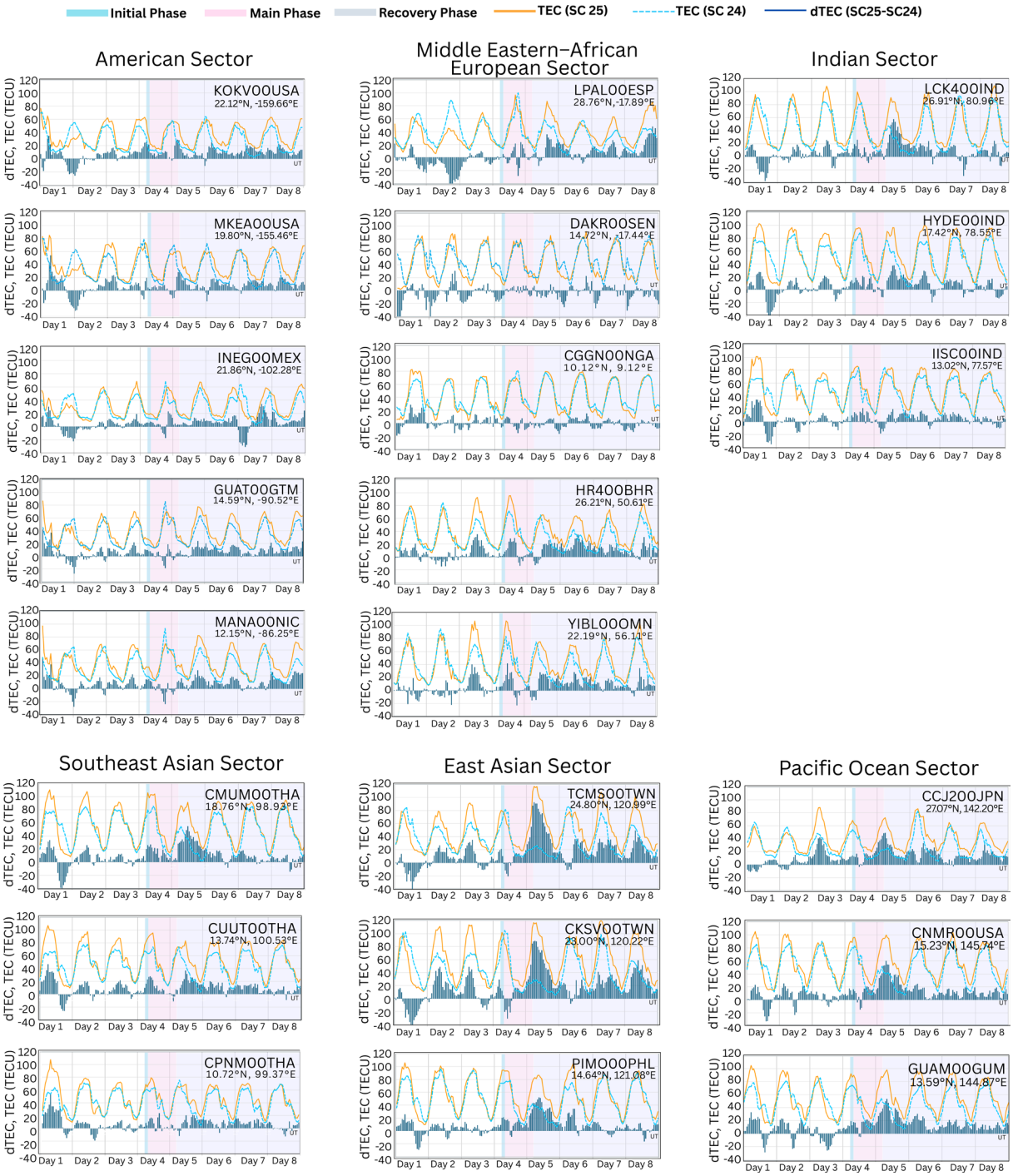

Figure 3. TEC and dTEC across 22 low-latitude IGS locations during geomagnetic storm events in SC24 and SC25. The data are grouped by locations and plotted against UT, highlighting differences in ionospheric response across longitudinal sectors.

disturbance than the SC24 event, despite their comparable geomagnetic storm intensities. Daily TEC disturbances were calculated relative to a quiet-time reference. Compared to SC25, the SC24 event exhibits more pronounced TEC depletion during the main and early recovery phases, highlighting solar-cycle-dependent differences in storm-time ionospheric responses, as shown in Fig. 5.

Daily TEC disturbances were calculated relative to a quiet-time reference. Compared to SC25, the SC24 event exhibits more pronounced TEC depletion during the main and early recovery phases, highlighting solar-cycle-dependent differences in storm-time ionospheric responses. (1) The American sector exhibits a mixed TEC response, characterized by both enhancements and depletions in ΔTEC. However, during the SC24 event, a more pronounced

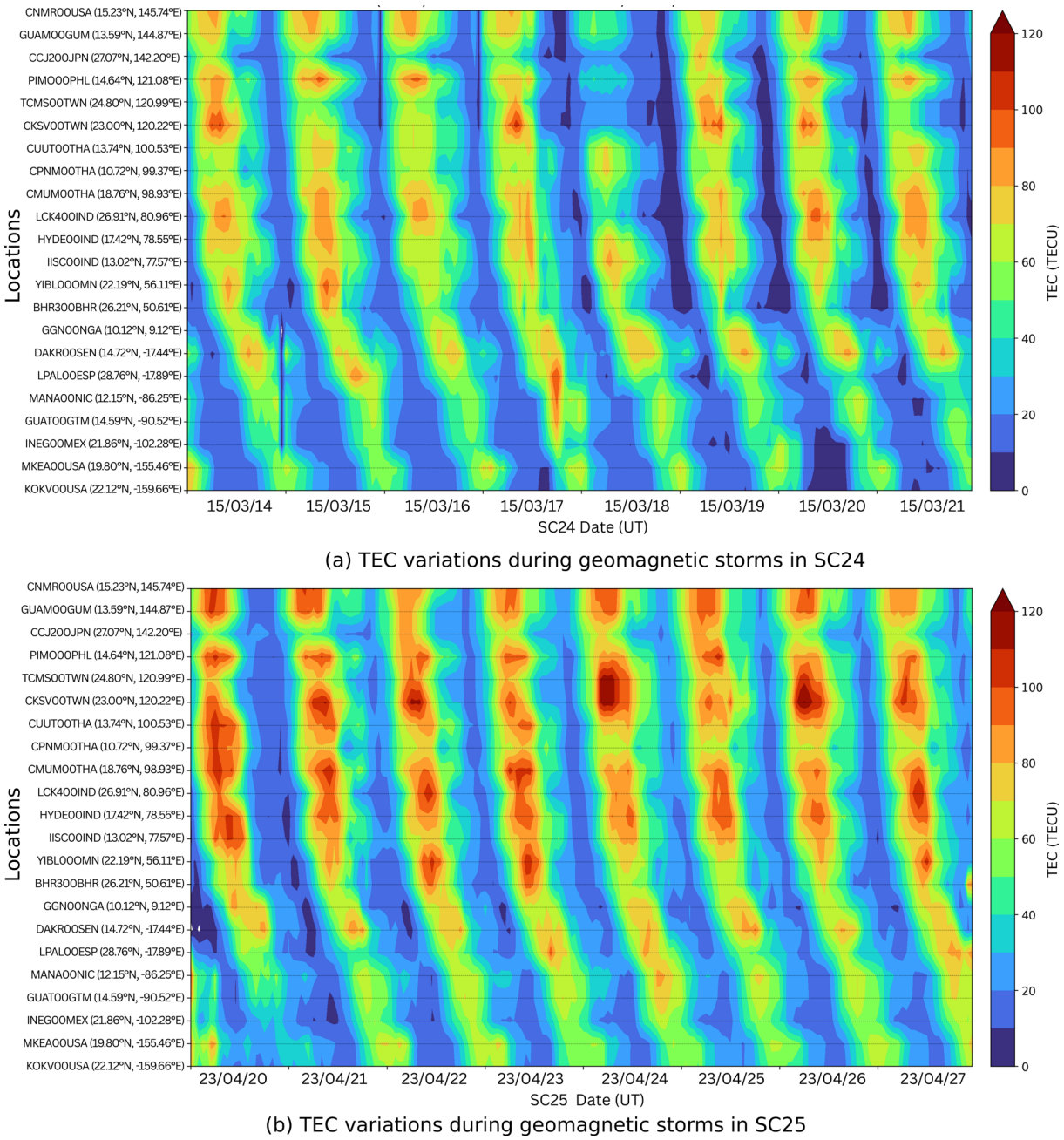

Figure 4. Comparison of spatiotemporal IONEX-derived TEC variations at 22 low-latitude IGS locations during geomagnetic storms in SCs 24 and 25.

positive response is observed in the main phase compared to other sectors. GUAT00GTM and MANA00NIC show markedly positive ΔTEC values (~+60 TECU). In contrast, during the SC25 event, the TEC variations continue to display clear diurnal oscillations, but the magnitudes of enhancement and depletion alternate, and the overall TEC increase is weaker than that observed in the East Asian and Pacific sectors. (2) In the Middle Eastern-African-European Sector region, the TEC response differs distinctly between the two storm events. During the main phase of SC24, several locations show a slight TEC enhancement. Conversely, during SC25, TEC values tend to decrease or exhibit only limited variation during the storm's most intense phase. Locations located at relatively higher latitudes, such as LPAL00 (Spain), display TEC enhancements during certain periods of both SC24 and SC25 relative to their quiet-time levels. This behavior likely reflects a poleward expansion or displacement of the EIA crest, allowing enhanced plasma densities to extend farther north, rather than a uniform increase in TEC across the entire sector. (3) The Indian sector demonstrates a clear contrast in ionospheric response between the two events. During SC24, a pronounced negative ionospheric storm is evident in the period following the main phase and into the early recovery

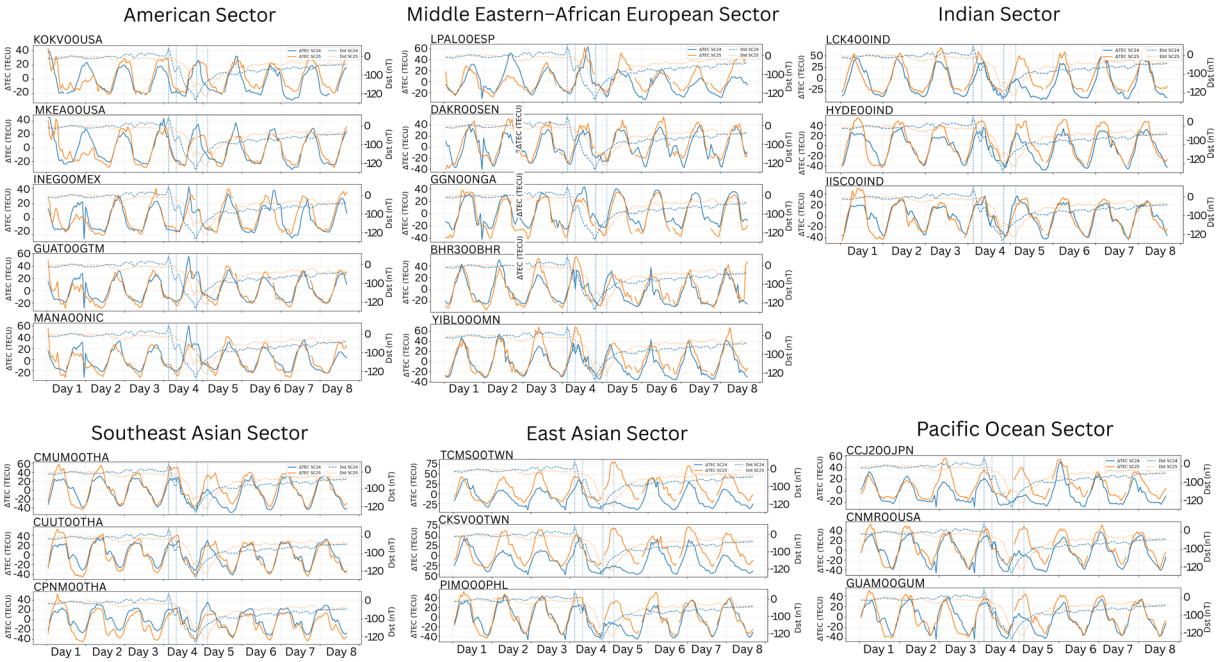

Figure 5. Hourly ΔTEC time series at low-latitude GNSS locations grouped by regional sectors, comparing SC24 and SC25 storms. The Dst index for SC24 (dashed) and SC25 (dotted) is overlaid on the right y-axis.

phase. In contrast, during SC25, ΔTEC values at locations LCK400IND and HYDE00IND remain persistently positive throughout the recovery phase (Days 6-8). This behavior suggests a denser accumulation of plasma over the Indian region and a slower ionospheric recovery than during SC24, even though the 2015 storm exhibited a lower minimum Dst value. (4) In the Southeast Asian sector, TEC responses differ markedly between the two storms. During the main phase (near the Dst minimum) of SC24, ΔTEC shows only a minor increase. In contrast, the SC25 event produces a much more pronounced TEC enhancement. Notably, the mid-latitude location CMUM00THA records TEC values exceeding 100 TECU during SC25, corresponding to ΔTEC (~+60 TECU), which is substantially higher than during SC24. Following the main phase of SC25, TEC recovery is observed at several locations, indicating a strong positive ionospheric response of the Southeast Asian region during the current solar cycle. (5) The East Asian sector exhibits the most pronounced TEC response during SC25, characterized by a strong and persistent positive ionospheric storm extending from the late main phase through the entire recovery phase. Near the Dst minimum of SC25, ΔTEC values at locations such as TCMS00TWN and CKSV00TWN reach approximately +75 TECU, representing the largest enhancements among all sectors. In contrast, during SC24, the East Asian sector shows a tendency toward negative ΔTEC near the peak storm intensity. This strong contrast between SC24 and SC25 highlights differences in storm-time electrodynamic driving mechanisms rather than differences in geomagnetic storm strength alone. (6) The Pacific Ocean sector displays a response pattern similar to that of the East Asian sector. During SC25, a pronounced positive ionospheric storm was observed, particularly during the recovery phase, with some intervals showing sustained positive ΔTEC values of approximately +40 TECU. In contrast, during SC24, the sector-averaged ΔTEC tends to be negative near the peak storm phase, reaching values of about −20 TECU. These results indicate that the Pacific sector is another region exhibiting a strong ionospheric response during SC25. Taken together, the Southeast Asian, East Asian, and Pacific sectors demonstrate a dominant positive response to the SC25 storm, whereas the Middle Eastern-African-European sector shows a comparatively weaker or negative response during the same period.

The present results reveal pronounced longitudinal and solar-cycle-dependent contrasts between the SC24 and SC25 geomagnetic storms. During SC25, TEC enhancements are substantially stronger and more persistent than during SC24, particularly across the Southeast Asian, East Asian, and Pacific sectors, where peak TEC values exceed those of SC24 by approximately 80-90 TECU near the storm main phase. These enhanced responses coincide with higher solar wind speeds (~650-700 km s^{-1}) and strongly fluctuating IMF Bz during SC25, which generated sustained and multi-pulse PPEFs. Such conditions favor intensified upward E × B drifts and a strengthened equatorial fountain effect, resulting in pronounced positive ionospheric storms. In contrast, SC24 was characterized by lower solar wind speeds (~550-600 km s^{-1}) and a more persistently southward IMF Bz, leading to shorter-lived PPEF forcing, weaker

TEC enhancement during the main phase, and pronounced TEC depletion during the recovery phase. The strong longitudinal dependence of storm-time TEC response is further supported by the correlation analysis between Dst and TEC disturbances. During the main phase of SC25, strong negative correlations dominate the Asia-Pacific sectors, indicating substantial TEC enhancement as geomagnetic storm intensity increased. Conversely, predominantly positive correlations are observed in the Middle Eastern-African-European sector, reflecting TEC depletion under intensified geomagnetic forcing. These contrasting patterns underscore the importance of local time, background ionization, and longitudinal electrodynamic coupling in regulating ionospheric responses, beyond storm intensity alone. The storm-time TEC responses observed in this study are consistent with earlier investigations demonstrating that ionospheric disturbances during geomagnetic storms are governed by the combined effects of storm-time electric fields, thermospheric composition changes, and strong spatial variability across latitude and longitude (Dabas et al., 2006; Nava et al., 2016). Early studies over the Indian region reported clear local-time dependence, with nighttime TEC depletion at equatorial latitudes and daytime enhancement at lower latitudes driven by disturbed electric fields and neutral winds (Dabas et al., 2006). Analyses of the March 17-18, 2015 St. Patrick's Day storm further highlighted latitudinal contrasts, showing TEC depletion at mid latitudes and enhancement near the equator (Nava et al., 2016). Subsequent studies demonstrated that daytime TEC enhancement during the storm main phase is primarily driven by PPEF-induced plasma uplift, followed by nighttime TEC depletion during the recovery phase under the influence of westward DDEFs (Yadav et al., 2016; Ray et al., 2017). The role of competing electric fields and neutral dynamics was further highlighted by Singh et al. (2021), who showed that TEC enhancements during sudden storm commencements are often followed by nighttime attenuation. Using multi-instrument observations, Berényi et al. (2023) demonstrated that changes in electric field orientation and plasma transport can simultaneously produce daytime enhancement and nighttime depletion, accompanied by equatorward expansion of the mid-latitude trough. Over East Africa, Habyarimana et al. (2023) reported TEC deviations exceeding 45% during the March 2015 storm, emphasizing strong regional sensitivity to storm-time electrodynamics. Recent studies have highlighted pronounced longitudinal and hemispheric differences during intense geomagnetic storms. Li et al. (2024) reported strong interhemispheric contrasts during the May 2024 superstorms, while Barad et al. (2025) confirmed significant TEC enhancement during the main phase of the April 2023 storm, followed by nighttime depletion during recovery and clear Asian-American sector asymmetries. Within this framework, TEC depletion has been shown to be highly region-dependent and controlled by the interplay between PPEFs, DDEFs, equatorial electrojet variability, and thermospheric composition changes (Vankadara et al., 2023; Chougule et al., 2025). Our results align with these findings and reveal clear contrasts between SC24 and SC25. In the Indian sector, TEC depletion is strongly modulated by the persistence of storm-time electric fields. Rajana et al. (2024) reported negative ionospheric storm effects during the recovery phase of the March-April 2023 storms due to dominant westward DDEFs. While our SC24 observations exhibit pronounced TEC depletion consistent with this mechanism, SC25 shows persistently positive ΔTEC at locations such as LCK400IND and HYDE00IND, indicating that intense and sustained PPEF pulses and enhanced background ionization during SC25 can counteract depletion processes (Chougule et al., 2025). TEC responses in the American sector are more heterogeneous. Localized post-sunset TEC depletions of ~22-45 TECU associated with equatorial plasma bubbles have been reported during SC25 (Vankadara et al., 2023), consistent with our observation that irregularity-driven depletions persist despite large-scale storm-time variability. In contrast, suppressed TEC depletion in the Southeast Asian and Pacific sectors during SC25 highlights the dominance of eastward PPEFs and enhanced background ionization under higher solar activity (Li et al., 2024; Barad et al., 2025). Focused studies of the April 2023 storm further support these interpretations. Tariq et al. (2024) showed that storm-time TEC responses were strongly controlled by the timing and polarity of electric fields relative to local time, with strong positive disturbances over the Asian-Australasian sector and weaker or negative responses over the American sector. Fashae and Fadiji (2025) reported equatorward displacement and partial collapse of the American EIA crests with TEC reduction, weak responses over Africa, and strong positive TEC enhancement (~30-35%) over the Asian-Australasian region. Rao et al. (2025) demonstrated that unusually strong and persistent storm-time electric fields over the Indian sector during the April 2023 storm, driven by highly fluctuating IMF Bz and enhanced solar wind speeds, intensified upward plasma transport and prolonged ionospheric disturbances into the recovery phase. Storm-time TEC responses are strongly dependent on local time, longitude, and storm-time electrodynamic forcing rather than geomagnetic storm intensity alone. Balan and Rao (1990) showed that the polarity and timing of ionospheric responses are largely controlled by the local time of sudden commencement. More recent studies, including Mohamed et al. (2023), further demonstrated pronounced longitudinal dependence and variable response delays. Overall, these results demonstrate that storm-time TEC variability is strongly longitude-dependent and

solar-cycle-dependent and cannot be explained by geomagnetic storm intensity alone. Instead, it is controlled by the complex interplay between PPEFs, DDEFs, local-time effects, and background ionospheric conditions, underscoring the need for integrated observational and modeling approaches to improve space weather prediction.

3.2 The relationship between geomagnetic storm intensity and TEC variations

The following table summarizes the correlation coefficients between different geomagnetic storm intensities, as represented by the Dst index, and GNSS TEC variations across 22 low-latitude locations during SC24 and SC25. The intensity of storms is divided into three phases: quiet phases, main phase, and recovery phase according to the Dst index. We used the interpretation of the size of a correlation coefficient as described by Mukaka (2012). This analysis highlights differences in TEC response across storm intensity and the solar cycle, as shown in Table 2.

Table 2. The relationship between geomagnetic storm intensity and the TEC variations in SC24 and SC25.

Correlation Coefficient / GNSS Locations	SC24			SC25		
	Quiet Time	Main phase	Recovery phase	Quiet Time	Main phase	Recovery Phase
KOKV00USA	−0.020	−0.690	−0.024	−0.499	−0.640	0.178
MKEA00USA	−0.018	−0.717	−0.035	−0.485	−0.550	0.153
INEG00MEX	0.159	−0.651	0.044	−0.531	−0.328	0.230
GUAT00GTM	0.176	−0.741	0.064	−0.424	−0.335	0.191
MANA00NIC	0.178	−0.725	−0.033	−0.347	−0.332	0.133
LPAL00ESP	0.214	0.117	0.013	0.026	0.592	0.102
DAKR00SEN	0.252	0.398	0.087	0.068	0.808	0.112
CGGN00NGA	0.100	0.578	0.050	0.337	0.979	−0.087
BHR400BHR	−0.173	0.794	−0.064	0.345	0.843	−0.176
YIBL00OMN	−0.125	0.828	0.007	0.326	0.815	−0.179
IISC00IND	−0.086	0.904	−0.100	0.348	0.764	−0.314
HYDE00IND	−0.130	0.932	0.064	0.346	0.765	−0.292
LCK400IND	−0.196	0.961	0.215	0.297	0.633	−0.283
CMUM00THA	−0.142	−0.791	0.224	0.296	−0.509	−0.326
CPNM00THA	−0.156	−0.691	−0.084	0.355	−0.373	−0.323
CUUT00THA	−0.127	−0.554	0.035	0.329	−0.488	−0.298
CKSV00TWN	−0.288	−0.835	0.080	0.164	−0.563	−0.375
PIMO00PHL	−0.182	−0.642	0.250	0.243	−0.336	−0.293
TCMS00TWN	−0.300	−0.834	0.098	0.106	−0.797	−0.516
CCJ200JPN	−0.260	−0.664	−0.027	−0.245	−0.520	−0.184
GUAM00GUM	−0.208	−0.431	0.100	0.174	−0.506	−0.264
CNMR00USA	−0.232	−0.569	0.138	0.151	−0.487	−0.282

Table 2 presents the Pearson correlation coefficients (r) between geomagnetic storm intensity, represented by the Dst index, and TEC variations during the quiet, main, and recovery phases for SC24 and SC25 across 22 IGS locations. In this analysis, a negative correlation ($r < 0$) indicates that TEC tends to increase as Dst becomes more negative, corresponding to a positive ionospheric storm response. Conversely, a positive correlation ($r > 0$) indicates that TEC tends to decrease as Dst becomes more negative, corresponding to a negative ionospheric storm response. Correlation strength is interpreted following Mukaka (2012). During the quiet phase, most locations in both cycles exhibit negligible correlations (generally $|r| < 0.3$), indicating that TEC variability under quiet conditions is weakly related to Dst and is dominated by regular drivers such as solar radiation and diurnal electrodynamics rather than geomagnetic forcing. In SC24, quiet-phase correlations are mostly small (e.g., TCMS00TWN −0.300; CKSV00TWN −0.288), while several locations in the American and the Middle Eastern-African-European sectors show negligible positive correlations (e.g., DAKR00SEN 0.252; LPAL00ESP 0.214). A distinctly different response pattern emerges during the main phase. In SC24, several locations in the American, the Southeast Asian, and the East Asian sectors exhibit high negative correlations (e.g., KOKV00USA −0.690; MKEA00USA −0.717; INEG00MEX −0.651; GUAT00GTM −0.741; MANA00NIC −0.725; CMUM00THA −0.791; CPNM00THA −0.691; CKSV00TWN −0.835; TCMS00TWN −0.834), indicating pronounced TEC enhancement as storm intensity increases (Dst becomes more negative). In contrast, multiple locations, particularly in the Middle Eastern-African-European and the Indian sectors, show high to very high positive correlations (e.g., LCK400IND 0.961; HYDE00IND 0.932; IISC00IND 0.904; YIBL00OMN 0.828; BHR400BHR 0.794), implying TEC depletion under intensified geomagnetic conditions at these locations. Collectively, SC24 therefore shows strong longitudinal variability, with both positive- and negative-storm signatures depending on sector and location. For SC25, the relationships during the main phase are also diverse but exhibit a clear regional structure. The American, Southeast Asian, East Asian, and Pacific sectors show moderate to high negative correlations (e.g., KOKV00USA −0.640; MKEA00USA −0.550; CMUM00THA −0.509; CKSV00TWN −0.563; TCMS00TWN −0.797; CCJ200JPN −0.520; GUAM00GUM −0.506), indicating strong TEC enhancement as Dst becomes more negative. In contrast, many locations in the MEA and Indian sectors exhibit moderate to very high positive correlations (e.g., LPAL00ESP 0.592; DAKR00SEN 0.808; CGGN00NGA 0.979; BHR400BHR 0.843; YIBL00OMN 0.815; IISC00IND 0.764; HYDE00IND 0.765; LCK400IND 0.633), indicating TEC depletion during the most intense storm conditions. During the recovery phase, correlations in both solar cycles generally weaken and are mostly negligible to low ($r \leq 0.3$), indicating reduced coupling between TEC and Dst as storm-time electrodynamic forcing relaxes. In SC24, recovery-phase correlations are small and include both signs (e.g., near zero to low positive and negative). In SC25, recovery correlations are small and positive in the American sector but become more negative at several locations in the Indian/Asian sectors (e.g., IISC00IND −0.314; HYDE00IND −0.292; LCK400IND −0.283; CMUM00THA −0.326; CPNM00THA −0.323; CKSV00TWN −0.375; TCMS00TWN −0.516; CNMR00USA −0.282) suggesting that depletion-type responses persist into recovery at some longitudes. Overall, Table 2 confirms that the Dst-TEC relationship is strongly phase- and longitude-dependent, with SC24 and SC25 exhibiting distinct regional patterns in the sign and strength of storm-time coupling.

3.3 Variations of foF2

Temporal heatmaps of foF2 recorded at 22 low-latitude locations during the geomagnetic storm events in SC24 and SC25 are presented in Figs. 6 and 7. The heatmaps illustrate hourly variations in foF2 (MHz) during storm periods, with higher color intensities corresponding to higher ionospheric electron densities. Pronounced daytime enhancements are observed, reflecting the ionospheric response to geomagnetic activity and highlighting clear spatial and temporal variability across locations and longitude sectors. Overall, foF2 values during SC25 are consistently higher than those observed during SC24, indicating enhanced electron densities in the ionosphere. This enhancement is closely associated with increased TEC, as foF2 and TEC are directly related through electron concentration in the F-region. Therefore, indicate a stronger low-latitude ionospheric response during SC25 than during SC24.

Figure 6 shows that during the main phase of the geomagnetic storm (March 17, 2015), significant changes in foF2 were observed at several low-latitude and near-equatorial locations, particularly in the Indian, Southeast Asian, and East Asian sectors. At these locations, foF2 values increased markedly during the daytime, indicating an increase in the peak electron density of the F2 layer. This increase is consistent with storm-time plasma uplift driven by eastward PPEFs, which transport ionization to higher altitudes where recombination rates are lower. In contrast, locations located in the American sector, such as INEG00MEX, GUAT00GTM, and MANA00NIC, exhibited a decrease in foF2

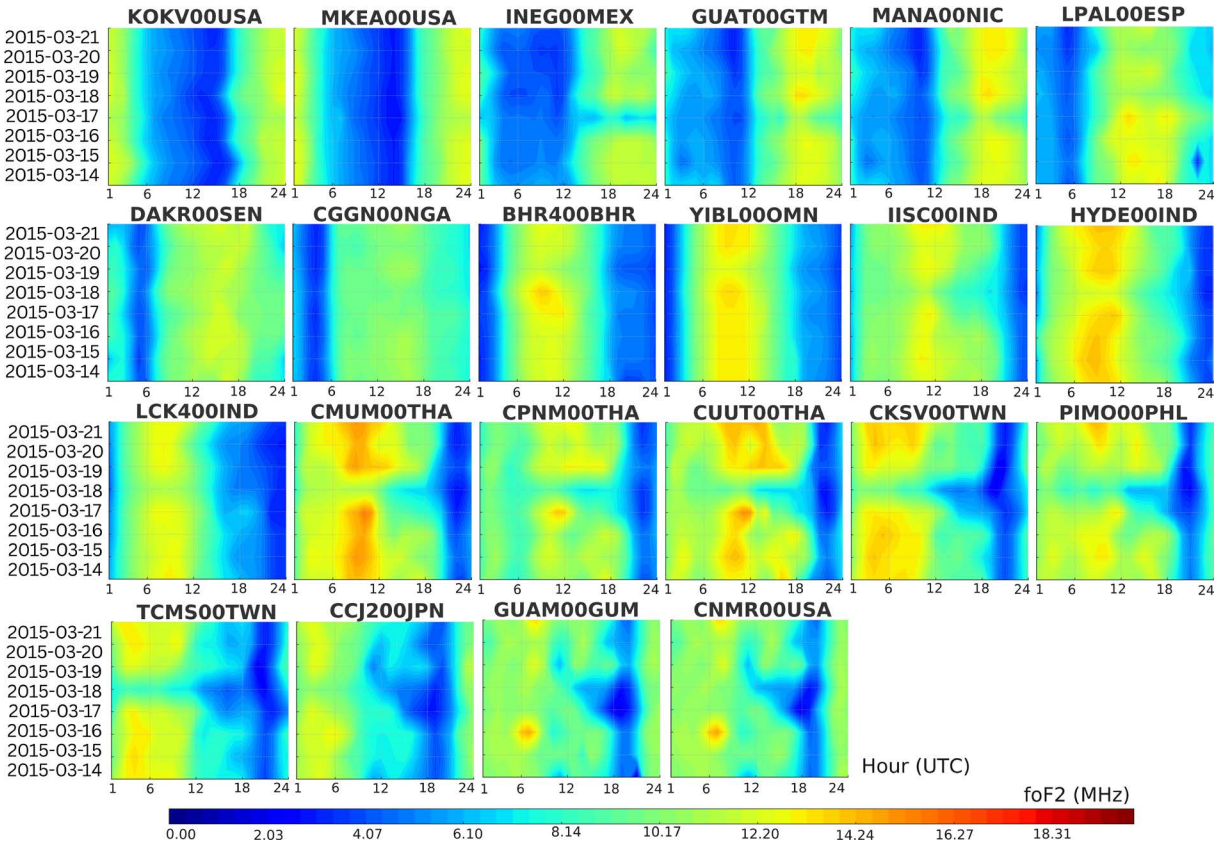

Figure 6. Temporal variations of foF2 at 22 low-latitude locations during the geomagnetic storm event in SC24.

during the storm main phase, suggesting regional differences in storm-time electrodynamic responses. During the recovery phase (March 18, 2015), many locations showed reduced daytime foF2 values and prolonged nighttime suppression compared to pre-storm conditions. Daytime foF2 remained lower at several locations, while nighttime minima became more pronounced. This behavior indicates a reduction in the peak electron density of the F2 layer and is consistent with the dominance of westward DDEFs and enhanced recombination processes during the recovery phase. Although partial recovery was observed at some locations, the overall foF2 levels remained disturbed. Notably, slight increases in foF2 were observed at locations such as BHR400BHR, YIBL00OMN, GUAT00GTM, and MANA00NIC, reflecting the prolonged impact of the geomagnetic storm on the low-latitude ionosphere. Furthermore, a comparison between the eight-day quiet-time average (March 14-16 and March 19-21) and the two storm-time days (March 17-18) reveals that most locations experienced a reduction in foF2 during the recovery phase. The percentage of Δ foF2's largest decreases was recorded at PIMO00PHL (−20.87%) and CKSV00TWN (−20.11%), followed by TCMS00TWN (−19.39%). Substantial reductions were also observed at CUUT00THA (−16.75%), CMUM00THA (−14.49%), INEG00MEX (−12.79%), CPNM00THA (−12.54%), GUAM00GUM (−12.82%), CNMR00USA (−12.06%), and CCJ200JPN (−10.54%), indicating a pronounced decrease in the F2-layer critical frequency under disturbed conditions. Moderate foF2 reductions, ranging from −5% to −10%, were found at IISC00IND (−9.31%), HYDE00IND (−6.90%), GUAT00GTM (−5.82%), and MANA00NIC (−5.98%). In contrast, smaller reductions (< −5%) were observed at MKEA00USA (−3.16%), LCK400IND (−3.11%), CGGN00NGA (−0.89%), and KOKV00USA (−0.04%), suggesting relatively weaker storm-time variability in these regions. Conversely, several locations exhibited increases in foF2 during the recovery phase, including BHR400BHR (6.64%), LPAL00ESP (3.67%), DAKR00SEN (2.97%), and YIBL00OMN (0.91%). These locations are predominantly located in the low-latitude Middle Eastern-African (MEA) region, extending into southern Europe, highlighting regional differences in ionospheric recovery behavior following the geomagnetic storm.

Generally, as shown in Fig. 7, foF2 values are higher during the daytime at each location, depending on local time, and lower at night. However, during geomagnetic storms, the normal diurnal pattern is distorted, and both enhancements and depletions of foF2 were observed, varying across different longitude sectors. During the main phase of the storm (April 23-24, 2023), pronounced increases in foF2 values were observed in several regions,

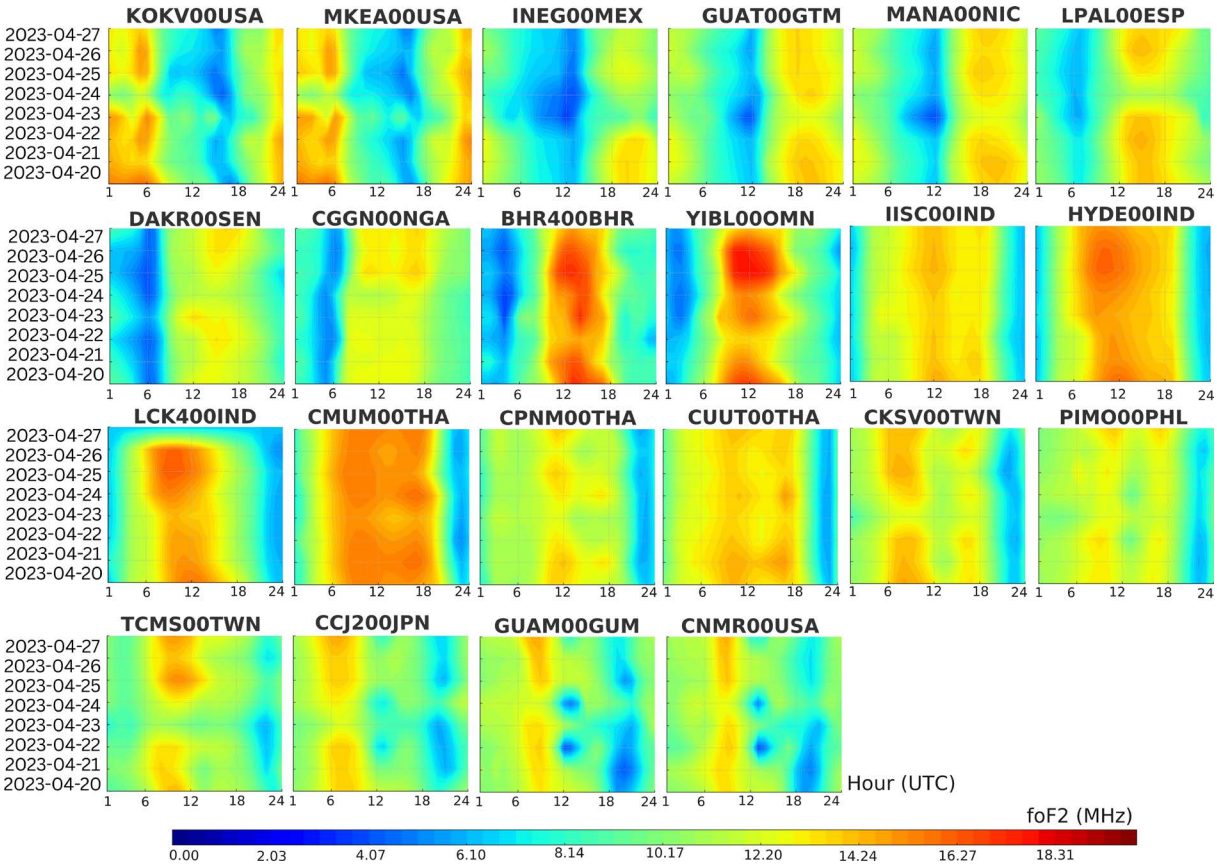

Figure 7. Temporal variations of foF2 at 22 low-latitude locations during the geomagnetic storm event in SC25.

particularly across the Indian, Southeast Asian, East Asian, and Pacific sectors, including locations such as LCK400IND, HYDE00IND, CMUM00THA, CUUT00THA, CPNM00THA, CKSV00TWN, and TCMS00TWN. These enhancements indicate an increase in NmF2, reflecting storm-time plasma uplift and the maintenance of elevated electron density in the F2 layer under the influence of disturbed electric fields and upper-atmospheric dynamics. In contrast, locations in the American sector (e.g., KOKV00USA, MKEA00USA, and INEG00MEX) and some locations at slightly higher latitudes (e.g., LPAL00ESP) do not show comparably strong increases in foF2 and, in some intervals, exhibit foF2 suppression. This behavior highlights a strong longitudinal dependence, whereby the same geomagnetic storm can produce positive ionospheric responses in some regions while inducing weak or negative responses in others, depending on local time and the dominant storm-time mechanisms. Meanwhile, in the MEA region, some locations, such as BHR400BHR and YIBL00OMN, display marked foF2 enhancements on certain days (April 23-24, 2023), indicating that this region experienced a relatively strong ionospheric response during specific intervals of the storm.

Following the main phase, during the recovery period (April 25-27, 2023), a transition toward recovery is observed. Many locations begin to reestablish a clearer day-night cycle; however, the diurnal pattern remains distorted compared to pre-storm conditions. Daytime foF2 values may remain elevated relative to baseline, while nighttime values remain suppressed. Moreover, at several locations, especially in the Asian-Pacific region and the MEA sector (e.g., BHR400BHR and YIBL00OMN), warm color signatures persist intermittently, indicating that ionospheric disturbances persist for several days after the main phase. This prolonged response suggests that, although recovery has commenced, the low-latitude ionosphere does not immediately return to quiet-time conditions. The strongest decrease in foF2 (% ΔfoF2) was detected at INEG00MEX (−19.62%). A reduction in foF2 in the range of −5% to −10% was found at TCMS00TWN (−10.59%), MANA00NIC (−9.83%) GUAT00GTM (−8.65%), LPAL00ESP (−7.46%), MKEA00USA (−6.92%), KOKV00USA (−6.16%), CKSV00TWN (−5.54%), and CCJ200JPN (−5.88%). A decrease smaller than −5% occurred at CGGN00NGA (−4.38%), YIBL00OMN (−3.12%), PIMO00PHL (−2.83%), CNMR00USA (−2.48%), CUUT00THA (−1.36%), CPNM00THA (−1.02%), CMUM00THA (−0.87%), HYDE00IND (−0.86), DAKR00SEN (−0.69%), GUAM00GUM (−0.68%), and BHR400BHR (−0.33%). In contrast, two locations exhibited positive storm-time responses, with increases recorded at LCK400IND (4.69%) and IISC00IND (0.10%).

The foF2 variations observed during the geomagnetic storm reveal a clear phase-dependent and longitudinally varying ionospheric response. During the main phase (April 23, 2023), pronounced daytime foF2 enhancements were detected at several low-latitude and near-equatorial locations in the Indian, Southeast Asian, East Asian, and Pacific sectors, indicating increased F2-layer peak electron density associated with storm-time plasma uplift driven by eastward PPEFs. In contrast, locations in the American sector exhibited foF2 reductions during the same phase, highlighting strong longitudinal dependence in storm-time electrodynamic forcing. Near the onset of the recovery phase (April 24, 2023), most locations showed reduced daytime foF2 values and prolonged nighttime suppression, with percentage changes indicating widespread foF2 depletion, particularly at PIMO00PHL, CKSV00TWN, TCMS00TWN, and INEG00MEX. These results indicate a substantial decrease in NmF2 during recovery, consistent with the dominance of westward DDEFs, enhanced recombination, and storm-induced thermospheric composition changes. Although partial recovery occurred at some locations, foF2 remained disturbed for several days, demonstrating the prolonged impact of the storm on the low-latitude ionosphere. Our findings are consistent with earlier studies reporting a decoupling between TEC and foF2 during geomagnetic storms. Previous investigations showed that daytime TEC enhancements can occur alongside foF2 reductions during the main phase, followed by negative ionospheric storm effects during recovery due to DDEFs (Yadav et al., 2016; Ray et al., 2017). Similar two-phase responses, characterized by initial positive effects and subsequent strong foF2 depletion, have also been reported over East Asia and other regions during the April 2023 storm (Bareh and Chetia, 2025; Barad et al., 2025). Overall, these results confirm that foF2 responses to geomagnetic storms are predominantly depletion-dominated, particularly during the recovery phase, and exhibit strong longitudinal variability. This highlights the sensitivity of foF2 to both storm-time electrodynamic forcing and thermospheric composition changes, underscoring the need for integrated observational and modeling approaches to fully understand storm-time ionospheric dynamics.

3.4 Variations of hmF2

The ionospheric F2-layer peak height (hmF2) variations during two geomagnetic storm events linked to SC24 (March 17-18, 2015) and SC25 (April 23-24, 2023) are compared in this study. The findings show apparent variations in the intensity and spatial distribution of the ionospheric responses. During SC24, the “St. Patrick’s Day storm” produced stronger but more localized disturbances, with hmF2 fluctuations exceeding 150 km at low- and mid-latitude locations. The SC25 storm, on the other hand, caused moderate but spatially broader responses, with hmF2 variations typically occurring over 50-100 km across multiple regions, especially over equatorial and low-latitude anomaly zones. These results imply that SC25 had a more widespread but moderate effect on ionospheric perturbations, whereas SC24’s geomagnetic forcing produced more intense, localized impacts. As shown in Figs. 8 and 9, the comparative findings shed new light on space weather variability and its regional dependencies, highlighting the impact of solar cycle intensity and geomagnetic driving mechanisms on global ionospheric dynamics.

In Fig. 8, during the pre-storm and quiet period, hmF2 exhibits a relatively stable diurnal pattern at most locations, characterized by moderate daytime peak heights and lower nighttime values. The spatial distribution of hmF2 remains fairly uniform across longitude sectors, indicating quiet-time electrodynamic conditions and a stable background ionosphere. During the main phase of the geomagnetic storm, noticeable changes in hmF2 are observed at several locations, particularly in the Indian, Southeast Asian, East Asian, and Pacific sectors. At these locations, hmF2 values increase during daytime hours, indicating an uplift of the F2-layer peak. However, the hmF2 response is not uniform across all regions. The American sector (e.g., KOKV00USA, MKEA00USA, and INEG00MEX) exhibits relatively weak hmF2 enhancements or nearly steady values, suggesting that storm-time electric-field penetration and local-time effects are less effective in producing F2-layer uplift in these regions. During the recovery phase, hmF2 values at most locations gradually decrease toward pre-storm levels, with reduced daytime peak heights and more pronounced nighttime lowering. This behavior reflects the diminishing influence of PPEFs and the increasing dominance of westward DDEFs, which suppress upward plasma transport and promote recombination at lower altitudes. Despite this general recovery trend, some locations, particularly in the Asian and Pacific sectors, continue to exhibit residual hmF2 disturbances, indicating that the ionosphere does not immediately return to quiet conditions after the storm subsides. Analysis of percentage hmF2 across 22 locations during the SC24 geomagnetic storm (March 17-18, 2015) reveals distinct temporal and spatial variations relative to the quiet-time baseline (six-day average excluding storm days). Overall, storm-time hmF2 exhibited both enhancements and suppressions depending on location. Mid- and low-latitude locations such as GUAM00GUM (8.25%), PIMO00PHL (5.87%), CCJ200JPN (5.41%), INEG00MEX (5.18%),

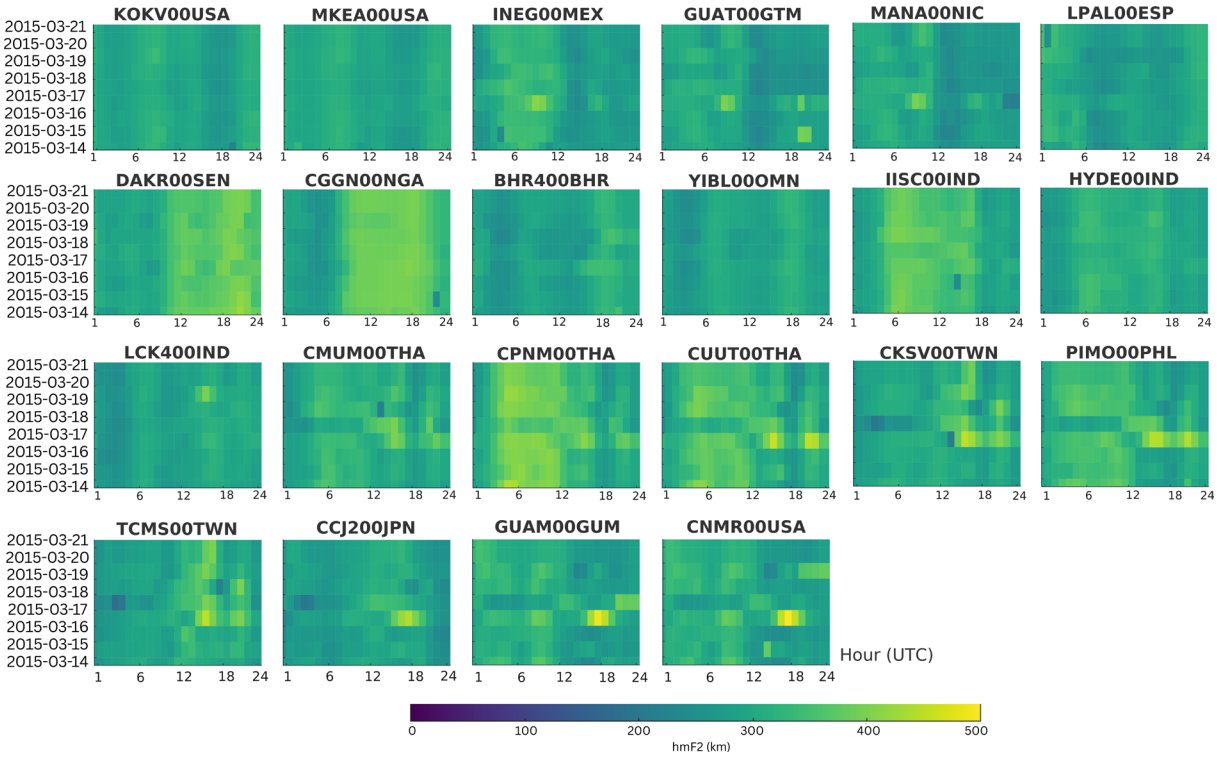

Figure 8. Temporal variations of hmF2 at 22 low-latitude locations during the geomagnetic storm event in SC24.

CNMR00USA (4.65%), CMUM00THA (4.47%), CUUT00THA (4.24%), GUAT00GTM (3.99%), MANA00NIC (3.56%), CKSV00TWN (3.49%), TCMS00TWN (3.41%), and CPNM00THA (2.99%) showed storm-time slight increases of ~3-8% relative to the quiet mean. By comparison, relatively negligible increases (~0-2%) were detected at IISC00IND (1.21%), LCK400IND (1.29%), BHR400BHR (1.85%), CGGN00NGA (0.62%), HYDE00IND (0.52%), LPAL00ES (0.38%), and YIBL00OMN (0.25%). Meanwhile, negligible decreases were observed at selected high-latitude and equatorial locations, including KOKV00USA (−1.49%), MKEA00USA (−0.35%), and DAKR00SEN (−0.13%).

During the pre-storm, relatively quiet period (Fig. 9), hmF2 exhibits a consistent diurnal pattern at most locations, with moderately elevated daytime values and lower nighttime heights. The spatial distribution of hmF2 is uniform across longitude sectors, indicating stable background ionospheric conditions and weak electrodynamic perturbations prior to storm onset. During the main phase of the geomagnetic storm (April 23-24, 2023), noticeable changes in hmF2 are observed across many locations, particularly in the Indian, Southeast Asian, East Asian, and Pacific sectors. At these locations, hmF2 values increase during daytime hours, indicating an uplift of the F2-layer peak. However, the hmF2 response is not spatially uniform. Locations in the American sector (e.g., KOKV00USA, MKEA00USA, and INEG00MEX) exhibit relatively weak hmF2 enhancement or near-steady values, suggesting that the effectiveness of storm-time electric field penetration and local-time coupling is reduced in these regions. In contrast, locations in the MEA region, such as BHR400BHR and YIBL00OMN, show pronounced hmF2 increases during certain intervals, indicating a strong local response to storm-time electrodynamic forcing. During the recovery phase (April 25-27, 2023), hmF2 values at most locations gradually decrease toward pre-storm levels. Daytime peak heights become lower, and nighttime hmF2 values decrease more clearly, reflecting the diminishing influence of PPEFs and the increasing dominance of westward DDEFs. These westward fields suppress upward plasma transport and enhance recombination at lower altitudes. Despite the overall recovery trend, residual hmF2 disturbances persist at several locations, particularly in the Asian and Pacific sectors and parts of the MEA region. This indicates that the low-latitude ionosphere does not return to quiet conditions immediately after the storm, highlighting the prolonged impact of geomagnetic disturbances during SC25. Analysis of hmF2 variations during the geomagnetic storm on April 23-24, 2023, at 22 locations revealed significant spatial and temporal variations relative to the average of the six-day quiet period. Overall, storm-time hmF2 responses were dominated by decreases, consistent with negative ionospheric storm phases at low- and mid-latitudes. In contrast, a subset of locations exhibited positive storm-time enhancements, with the largest increases recorded at BHR400BHR (4.30%), YIBL00OMN (4.27%), TCMS00TWN (3.26%), CCJ200JPN (3.22%),

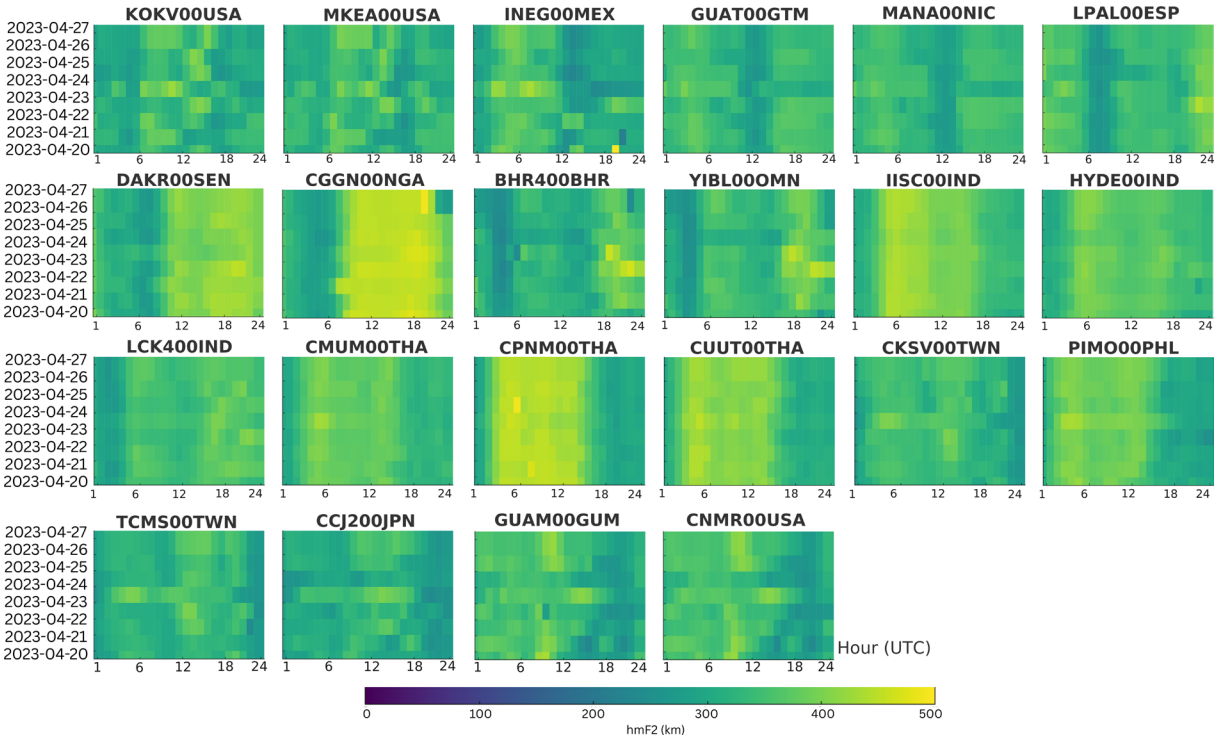

Figure 9. Temporal variations of hmF2 at 22 low-latitude locations during the geomagnetic storm event in SC25.

MKEA00USA (2.80%), KOKV00USA (2.71%), HYDE00IND (2.51%), CNMR00USA (1.85%), IISC00IND (1.49%), CKSV00TWN (1.45%), LPAL00ESP (1.44%), PIMO00PHL (0.90%), CGGN00NGA (0.87%), DAKR00SEN (0.73%), CMUM00THA (0.72%), MANA00NIC (0.58%), LCK400IND (0.57%) and GUAM00GUM (0.45%). The depletions were detected at INEG00MEX (−2.73%), CPNM00THA (−0.59%), GUAT00GTM (−0.40%), and CUUT00THA (−0.33%).

Significant temporal and spatial variability in the hmF2 response during geomagnetic storms reflects the interaction between electrodynamic forcing and changes in thermospheric composition. Analysis of Fig. 6 shows that during the storm on March 17-18, 2015 (SC24), low-latitude locations showed a slight increase in hmF2 of 3-8%, while only a few locations showed a slight decrease, indicating that the F2 peak increased locally. The maximum increase in hmF2 for the SC25 event was approximately three percentage points. This is consistent with Yadav et al. (2016), who observed that, despite the daytime TEC enhancement attributed to PPEF, hmF2 did not exhibit the expected uplift during the main phase over the Indian sector, suggesting suppressed plasma transport. Ray et al. (2017) also highlighted the complexity of this storm, noting that while PPEF-driven uplift increased TEC during the day, DDEF and composition effects dominated the recovery phase and led to negative ionospheric responses. This unexpected behavior demonstrates hmF2's high sensitivity to electrical forces and competing thermospheric forces. A significantly different hmF2 pattern was observed during the storms of April 23-24, 2023 (SC25), although there was also a local increase in intensity exceeding 1-3%, particularly in Central America and Southeast Asia. According to Barad et al. (2025) used TIE-GCM simulations and combined observations to validate these disparate regional responses. They showed that, while hmF2 showed a strong uplift in some regions during the main phase due to PPEF, the recovery phase was dominated by storm-time depressions associated with DDEF. Bareh and Chetia (2025), in their analysis of previous SC24 storms, emphasize the importance of storm intensity, phase, and geographic location in determining hmF2 variability. These results are consistent with Tariku (2024), who examined storm-time variations of TEC, foF2, and hmF2 from observations and empirical models (IRI 2016 and IRI-Plas 2017) across different latitudes and solar activity levels. The study reported positive storm effects during events on February 19, 2014, March 17, 2015, and November 4, 2021, particularly at low latitudes, whereas storms on September 8, 2017, and August 26, 2018, were dominated by negative effects at mid and high latitudes. The relationship between peak TEC and hmF2 was latitude- and solar-cycle dependent. Peak TEC coincided with increased hmF2 at low latitudes but was associated with decreased hmF2 at mid latitudes. During low solar activity, peak TEC was generally associated with hmF2 reductions, in contrast to the behavior during high solar activity. Both

IRI 2016 and IRI-Plas 2017 reproduced the overall TEC and hmF2 variations reasonably well, with modeled peak TEC occurring at hmF2 values comparable to observations. Collectively, these results indicate that, while hmF2 may show a brief uplift under PPEF forcing during the main phase, suppressions linked to disturbance dynamo effects and thermospheric composition typically dominate storm recovery phases. The divergent behavior across regions and solar cycles emphasizes the need for multi-instrument and model-based approaches to unravel the complex coupling processes governing F2-layer peak height during geomagnetic storms.

4. Conclusions

Although the geomagnetic storms in SC24 (March 17-18, 2015) and SC25 (April 23-24, 2023) reached comparable minimum Dst values (−223 nT and −212 nT, respectively), the ionospheric responses observed during these two events differ substantially in magnitude, spatial extent, and persistence. These differences can be fundamentally attributed to differences in the temporal structure of IMF Bz and V, and in the resulting PPEFs. In SC24, the storm main phase was driven by a sustained and strongly southward IMF Bz, accompanied by moderately enhanced solar wind speeds (~550-600 km s^{-1}). This configuration enabled efficient, continuous solar wind-magnetosphere coupling, leading to rapid intensification of the ring current and a sharp decrease in Dst. However, the southward Bz interval was relatively coherent and less fluctuating; the associated PPEF signatures were short-lived and sporadic, rather than persistent. Consequently, the eastward electric field's penetration into the low-latitude ionosphere was brief, reducing the cumulative impact of upward ExB plasma drifts. This explains why, despite the strong geomagnetic forcing, SC24 produced weaker and more localized TEC enhancements, modest hmF2 uplift, and widespread foF2 depletion during the recovery phase. In contrast, the SC25 storm was characterized by higher solar wind speeds (~650-700 km s^{-1}) combined with a highly fluctuating IMF Bz, which alternated rapidly between southward and northward orientations. This variability repeatedly disrupted magnetospheric shielding, producing alternating periods of undershielding and overshielding. As a result, PPEFs were generated in multiple, strong pulses, persisting throughout much of the storm's main phase. These multi-pulse PPEFs played a crucial role in sustaining enhanced eastward electric fields at low latitudes over extended periods. The prolonged PPEF forcing during SC25 significantly enhanced upward plasma transport in the equatorial F region, strengthening the equatorial fountain effect and redistributing plasma toward low-latitude anomaly crests. This mechanism explains the large, spatially coherent TEC enhancements, the pronounced daytime increases in foF2, and the moderate hmF2 uplift observed across the Indian, Southeast Asian, East Asian, and Pacific sectors during SC25. Importantly, the coincidence of PPEF pulses with favorable local-time conditions further amplified the ionospheric response in these longitude sectors. Another key distinction between the two storms lies in their electrodynamics during the recovery phase. In SC24, the recovery phase was dominated by westward DDEFs and storm-induced changes in thermospheric composition. These processes suppressed upward plasma transport, enhanced recombination at lower altitudes, and produced negative ionospheric storm effects, evident as TEC depletion, foF2 reduction, and declining hmF2 at most locations. The persistence of negative Dst values during recovery indicates a slow decay of the ring current, further reinforcing these suppressive mechanisms. By contrast, although DDEFs also developed during the SC25 recovery phase, their impact was partially offset by the enhanced background ionization associated with higher solar activity in Solar Cycle 25 and by the residual effects of earlier PPEF-driven uplift. Consequently, TEC levels in several regions, particularly the Indian and Asian-Pacific sectors, remained elevated well into the recovery phase, even as foF2 and hmF2 began to decrease. This behavior highlights a partial decoupling between TEC and foF2, in which the total electron content remains high due to plasma redistribution and retention, while the F2-layer peak density and height respond more sensitively to recombination and composition-driven processes. Taken together, these results demonstrate that storm-time ionospheric responses are controlled not only by storm intensity (Dst), but more critically by the temporal variability of IMF Bz and the persistence of PPEF forcing. SC25 illustrates how higher solar wind speeds combined with fluctuating Bz can sustain prolonged electrodynamic forcing, producing stronger and more widespread ionospheric disturbances than a storm with a more intense but temporally compact southward IMF, as observed in SC24. This finding underscores the importance of considering Bz variability and PPEF structure, rather than Dst magnitude alone, when assessing and forecasting low-latitude ionospheric impacts during geomagnetic storms. It should be noted that uncertainties associated with GIM-derived TEC and GAMBIT-derived foF2 and hmF2, arising from data coverage, assimilation procedures, and model assumptions, represent limitations of this study. These uncertainties may affect quantitative estimates but do not alter the main conclusions regarding longitudinal dependence, electrodynamic forcing, and solar-cycle-related ionospheric responses.

Data availability statement. The ionosonde-derived foF2 and hmF2 data used in this study are available from the Global Ionospheric Radio Observatory (GIRO) at https://giro.uml.edu/rix/gambit-local-nowcast/. The IONosphere Map EXchange (IONEX) files can be accessed through NASA's Crustal Dynamics Data Information System (CDDIS) at https://cddis.nasa.gov/archive/gnss/products/ionex/YYYY/DDD/. Hourly Dst index values were obtained from the World Data Center for Geomagnetism, Kyoto (https://wdc.kugi.kyoto-u.ac.jp/dst_provisional/index.html). The Kp index data were retrieved from the NOAA Space Weather Prediction Center (SWPC) (https://www.swpc.noaa.gov/) and the Pushkov Institute of Terrestrial Magnetism, Ionosphere, and Radio Wave Propagation (IZMIRAN) (https://www.izmiran.ru/ionosphere/weather/storm/).

Acknowledgements. We sincerely acknowledge the Global Ionospheric Radio Observatory (GIRO) for providing foF2 and hmF2 ionosonde data. We also thank NASA's Crustal Dynamics Data Information System (CDDIS) for access to the IONosphere Map Exchange (IONEX) files. The authors are grateful to the World Data Center for Geomagnetism, Kyoto, for providing hourly Dst index values, and to the NOAA Space Weather Prediction Center (SWPC) and the Pushkov Institute of Terrestrial Magnetism, Ionosphere, and Radio Wave Propagation (IZMIRAN) for providing Kp index data. The authors gratefully acknowledge King Mongkut's Institute of Technology Ladkrabang (KMITL) and Rajamangala University of Technology Thanyaburi (RMUTT) for their generous support and valuable assistance throughout this research.

References

Balan, N. and P. B. Rao (1990). Dependence of ionospheric response on the local time of sudden commencement and the intensity of geomagnetic storms. Journal of Atmospheric and Terrestrial Physics, 52, 4, 269-275, doi:10.1016/0021-9169(90)90094-4.

Barad, R. K., S. Sripathi, R. Singh, B. Gayathri and P. Abadi (2025). Observations and modeling investigations of ionospheric response to 23-24 April 2023, G4-class geomagnetic storm over Indian sector, Space Weather, 23(e2024SW00425), doi:10.1029/2024SW004253.

Bareh, A. and B. Chetia (2025). Comprehensive analysis of the ionospheric response to the 2015 geomagnetic storms over different station, Atmo. Climate Sci., 15(1), 175-186, doi:10.4236/acs.2025.151008.

Berényi, K. A., B. Heilig, J. Urbář, D. Kouba et al. (2023). Comprehensive analysis of the ionospheric response to the largest geomagnetic storms from solar cycle 24 over Europe. Frontiers in Astronomy and Space Sciences, 10(1092850), 1-22. doi:10.3389/fspas.2023.1092850.

Can, Z. and H. Ş. Erdağ (2025). Effect of Solar parameters on geomagnetic storm formation in the ascending phase of the 25th Solar Cycle, Solar Phys., 300, 20, doi:10.1007/s11207-025-02427-x.

Chernyshov, A. A., W. J. Miloch, Y. Jin and V. I. Zakharov (2020). Relationship between TEC jumps and auroral substorm in the high-latitude ionosphere, Sci. Rep., 10, 6363, 1-13, doi:10.1038/s41598-020-63422-9.

Chougule, P., D. Shetti, K. Venkatesh, G. K. Seemala and S. Chougule (2025). A study of the ionospheric response during intense geomagnetic storms over the Indian low-latitude region during the period 2017-2023, Adv. Space Res. doi:10.1016/j.asr.2025.09.088.

Dabas, R. S., L. Singh, S. C. Garg, R. M. Das, K. Sharma and V. K. Vohra (2006). Growth and decay of a post-sunset equatorial anomaly at low latitudes: Control of E × B, neutral winds and daytime electrojet strength. Journal of Atmospheric and Solar-Terrestrial Physics, 68(14), 1622-1632. doi:10.1016/j.jastp.2006.05.020.

Dias, M. A. L., P. R. Fagundes, K. Venkatesh, V. G. Pillat et al. (2020). Daily and monthly variations of the equatorial ionization anomaly (EIA) over the Brazilian sector during the descending phase of the Solar Cycle 24, J. Geophys. Res.: Space Phys., 125, e2020JA027906, doi:10.1029/2020JA027906.

Fashae, J. B. and J. O. Fadiji (2025). Response of low-latitude ionosphere to 24 April 2023 geomagnetic storm over the American, African, and Asian-Australian sectors. Canadian Journal of Physics, 103, 7, 654-668. doi:10.1139/cjp-2024-0225.

Gordiyenko, G., F. Arikan, Y. Litvinov and M. Zhiganbaev (2025). Ionospheric response to the extreme geomagnetic storm of 10 -11 May 2024 based on total electron content observations in the Central Asian and East Asian Regions, Atmosphere, 16, 7, 854, 1-14, doi:10.3390/atmos16070854.

Habyarimana, V., J. B. Habarulema and T. Dugassa (2023). Analysis of ionospheric storm-time effects over the East African sector during the 17 March 2013 and 2015 geomagnetic storms, Earth, Planets and Space, 75, 58, doi:10.1186/s40623-023-01812-9.

Hofmann-Wellenhof, B., H. Lichtenegger and J. Collins (1992). GPS – Global Positioning System: Theory and practice (5th edition), Springer-Verlag, doi:10.1007/978-3-7091-5126-6.

Kenpankho, P., P. Supnithi, T. Tsugawa and T. Maruyama (2011). Variation of ionospheric slab thickness observations at Chumphon equatorial magnetic location, Earth, Planets and Space, 63, 359-364, doi:10.5047/eps.2011.03.003.

Kim, J.- H. and Y.- S. Kwak (2025). Validating the IRI-2020 model for ionospheric storms over the North-East Asian sector induced by extreme geomagnetic storms, Adv. Space Res., 75, 5, 4347-4369, doi:10.1016/j.asr.2024.07.032.

Lazzús, J. A., I. Salfate and P. Vega-Jorquera (2022). Intense geomagnetic storms in the maximum phase of Solar Cycle 24 observed from a low-latitude ground station, Geofísica internacional, 61, 4, 267-286, doi:10.22201/igeof.00167169p.2022.61.4.2028.

Li, G., B. Ning, X. Zhao, W. Sun et al. (2019). Low latitude ionospheric TEC oscillations associated with periodic changes in IMF Bz polarity, Geophys. Res. Lett., 46, 16, 9379-9387, doi:10.1029/2019GL084428.

Li, W. B., L. B. Liu, Y. Y. Yang, T. W. Han et al. (2024). Interhemispheric and longitudinal differences in the ionosphere-thermosphere coupling process during the May 2024 superstorm, Earth Planet. Phys., 8 6, 910-919, doi:10.26464/epp2024073.

Mohamed, H. S., C. Amory-Mazaudier, S. K. Panda, O.M. Shalabiea and A. Mahrous (2023). Delayed response of low latitudes TEC during thirty-six geomagnetic storms from 2014 to 2017, J. Atmosph. Solar-Terr. Phys., 250,106109, doi:10.1016/j.jastp.2023.106109.

Mošna, Z., V. Barta, K. A. Berényi, J. Mielich et al. (2024). The March and April 2023 ionospheric storms over Europe. Front. Astron. Space Sci., 11, 1462160, doi:10.3389/fspas.2024.1462160.

Mukaka, M. M. (2012). Statistics corner: A guide to appropriate use of correlation coefficient in medical research, Malawi Medical Journal, 24, 3, 69-71, PMID: 23638278.

Nava, B., J. Rodríguez-Zuluaga, K. Alazo-Cuartas, A. Kashcheyev et al. (2016). Middle- and low-latitude ionosphere response to 2015 St. Patrick's Day geomagnetic storm, J. Geophys. Res.: Space Phys, 121, 4, 3421-3438, doi:10.1002/2015JA022299.

Nayak, C., L. C. Tsai, S. Y. Su, I. A. Galkin et al. (2016). Peculiar features of the low latitude and midlatitude ionospheric response to the St. Patrick's Day geomagnetic storm of 17 March 2015, J. Geophys. Res.: Space Phys., 121, 8, 7941-7960, doi:10.1002/2016JA022489.

Pansong, C., P. Wongsak, S. Ruttanaburee, P. Pornsopin and P. Kenpankho (2025). Low latitude TEC disturbances during extreme geomagnetic storms: Insights into March and May 2024, Adv. Space Res., 76, 12, 7521-7532, doi:10.1016/j.asr.2025.03.071.

Paul, K. S., H. Haralambous, M. Moses, C. Oikonomou et al. (2025). Investigation of the ionospheric response on Mother's Day 2024 geomagnetic superstorm over the European Sector, Atmosphere, 16, 2, 180, doi:10.3390/atmos16020180.

Pesnell, W. D. (2016). Predictions of solar cycle 24: How are we doing?, Space Weather, 14, 1, 10-21 doi:10.1002/2015SW001304.

Pi, X., A. J. Mannucci, U. J. Lindqwister and C. M. Ho (1997). Monitoring of global ionospheric irregularities using the worldwide GPS network, Geophys. Res. Lett., 24, 18, 2283-2286, doi:10.1029/97GL02273.

Picanço, G. A. S., C. M. Denardini, P. A. B. Nogueira, L. C. A. Resende et al. (2022). Study of the equatorial and low-latitude total electron content response to plasma bubbles during solar cycle 24-25 over the Brazilian region using a Disturbance Ionosphere IndeX, Ann. Geophysicae, 40, 4, 503-517, doi:10.5194/angeo-40-503-2022.

Rajana, S. S. K., S. K. Panda, S. Jade, C. G. Vivek et al. (2024). Impact of two severe geomagnetic storms on the ionosphere over Indian longitude sector during March-April 2023, Astrophys. Space Sci., 369, 3, doi:10.1007/s10509-024-04268-9.

Ray, S., B. Roy, K. S. Paul and S. Goswami (2017). Study of the effect of 17-18 March 2015 geomagnetic storm on the Indian longitudes using GPS and C/NOFS, J. Geophys. Res.: Space Phys., 122, 2, 2551-2563, doi:10.1002/2016JA023127.

Reddybattula, K. D., S. K. Panda, K. Ansari and V. S. R. Peddi (2019). Analysis of ionospheric TEC from GPS, GIM and global ionosphere models during moderate, strong, and extreme geomagnetic storms over Indian region, Acta Astronautica, 161, 283-292, doi:10.1016/j.actaastro.2019.05.042.

Reinisch, B. W and I. A. Galkin (2011). Global ionospheric radio observatory (GIRO), Earth, Planets, and Space, 63, 377-381, doi:10.5047/eps.2011.03.001.

Reyes, P. I., V. A. Pinto and P. S. Moya (2021). Geomagnetic storm occurrence and their relation with solar cycle phases, Space Weather,19(e2021SW002766), doi:10.1029/2021SW002766.

Rao, S. S., N. Srivastava and D. Chakrabarty (2025). Variation in horizontal component of geomagnetic field during the April 2023 space weather event over longitude sectors: Insights, J. Astrophys. Astron., 46, 37, doi:10.1007/s12036-025-10066-8.

Rukundo, W. (2023). The ionospheric dynamics of the African sector responding to a severe geomagnetic storm; the storm of 3-5 November 2021. Space Weather, 21(e2022SW003219), doi:10.1029/2022SW003219.

Serafimov, K. B., I. S. Arshinkov, A. Z. Bochev, M. H. Petrunova et al. (1982). A measuring equipment for electric and magnetic fields in the range of the ionosphere-magnetosphere plasma mounted aboard the "Intercosmos-Bulgaria 1300" satellite, Acta Astronautica, 9, 6-7, 397-399, doi:10.1016/0094-5765(82)90068-6.

Singh, A., V. S. Rathore, S. Kumar, S. S. Rao et al. (2021). Effect of intense geomagnetic storms on low-latitude TEC during the ascending phase of the solar cycle 24, J. Astrophys. Astron., 42, 99, doi:10.1007/s12036-021-09774-8.

Skone, S. and M. de Jong (2000). The impact of geomagnetic substorms on GPS receiver performance. Earth, Planets and Space, 52, 1067-1071. doi:10.1186/BF03352332.

Solomon, S. C., T. N. Woods, L. V. Didkovsky, J. T. Emmert and L. Qian (2010). Anomalously low solar extreme-ultraviolet irradiance and thermospheric density during solar minimum, Geophys. Res. Lett., 37, 16, L16103, doi:10.1029/2010GL044468.

Tariku, Y. A. (2024). The geomagnetic storm time responses of the TEC, foF2, and hmF2 in different solar activity during Solar Cycle 24 and 25, Radio Sci., 59, 12, e2024RS007961, doi:10.1029/2024RS007961.

Tariq, A. M., L. Liu, M. Shah, Y. Yang et al. (2024). Longitudinal variations of ionospheric responses to the February and April 2023 geomagnetic storms over American and Asian sectors, Adv. Space Res., 73, 6, 3033-3049, doi:10.1016/j.asr.2023.12.039.

Tilahun, A. M., E. Uluma and Y. G. Ejigu (2025). Variation in Total Electron Content during a severe geomagnetic storm, 23-24 April 2023, Atmosphere, 16, 6, 676, doi:10.3390/atmos16060676.

Timoçin, E. (2019). The effect of different phases of severe geomagnetic storms on the low latitude ionospheric critical frequencies, Adv. Space Res., 64,11, 2280-2289. doi:10.1016/j.asr.2019.08.026.

Uga, C. I., S. P. Gautam and E. B. Seba (2024). TEC disturbances caused by CME-triggered geomagnetic storm of September 6-9, 2017, Heliyon,10, 10, e30725, doi:10.1016/j.heliyon.2024.e30725.

Vankadara, R. K., P. Jamjareegulgarn, G. K. Seemala et al. (2023). Trailing equatorial plasma bubble occurrences at a low-latitude location through Multi-GNSS slant TEC fepletions during the strong geomagnetic storms in the ascending phase of the 25th Solar Cycle, Remote Sensing, 15, 20, 4944. doi:10.3390/rs15204944.

Wang, Y., Y. Yuan, M. Li, T. Zhang et al. (2023). Effects of strong geomagnetic storms on the ionosphere and degradation of precise point positioning accuracy during the 25th Solar Cycle rising phase: A case study, Remote Sensing, 15, 23, 5512, doi:10.3390/rs15235512.

Wu, C. C., K. Liou, R. P. Lepping, L. Hutting et al. (2016). The first super geomagnetic storm of solar cycle 24: "The St. Patrick's day event (17 March 2015)", Earth, Planets and Space, 68, 151, doi:10.1186/s40623-016-0525-y.

Yadav, S., S. Sunda and R. Sridharan (2016). The impact of the 17 March 2015 St. Patrick's Day storm on the evolutionary pattern of equatorial ionization anomaly over the Indian longitudes using high-resolution spatiotemporal TEC maps: New insights, Space Weather, 14, 10, 786-801. doi:10.1002/2016SW001408.

Zhao, D., S. Cui, X. Zhang, L. Li et al. (2024). Analysis of global ionospheric scintillation and GPS positioning interference triggered by full-halo CME-driven geomagnetic storm: A case study, Adv. Space Res., 74, 5, 2492-2509, doi:10.1016/j.asr.2024.06.001.

Zhu, Q., Lu, G. and Y. Deng (2022). Low and mid-latitude ionospheric response to the 2013 St. Patrick's Day geomagnetic storm in the American sector: Global ionosphere thermosphere model simulation. Frontiers in Astronomy and Space Sciences, 9, 916739, 1-15 doi:10.3389/fspas.2022.916739.

***CORRESPONDING AUTHOR: Prasert KENPANKHO**,
King Mongkut's Institute of Technology Ladkrabang, School of Industrial Education and Technology,
Department of Engineering Education, Bangkok, Thailand
e-mail: prasert.ke@kmitl.ac.th